Synergistic effect of microstructure and defects on the initiation of fatigue cracks in additively manufactured Inconel 718

Mohammad S. Dodaran, Muztahid Muhammad, Nima Shamsaei, Shuai Shao [*]

National Center for Additive Manufacturing Excellence (NCAME), Auburn University, Auburn, AL 36849, USA
Department of Mechanical Engineering, Auburn University, Auburn, AL 36849, USA

ARTICLE INFO

ABSTRACT

Fatigue cracks in additively manufactured (AMed) Inconel 718 (IN-718) in machined surface condition often initiate from persistent slip bands (PSBs) unlike other popular AM alloys such as 17-4 PH stainless steel or Ti-6Al-4V, where fatigue crack initiation is exclusively from volumetric defects; therefore, a competition between PSB- vs. defect- mediated crack initiation clearly exists. To shed light on the factors governing the competition, this study investigates the characteristics of cyclic strain localization, PSB formation, and crack initiation via crystal plasticity (CP) modeling of cyclic loading on polycrystalline aggregates which are then validated by experiments. A physics-based, free slip distance (FSD) dependent slip strength evolution law is proposed, which is shown to enable the CP model to simulate the heterogeneous strain distribution in IN-718. Implementing a crack initiation criterion based on strain contrast, the locations and lives for crack initiation can also be calculated. It is shown that both FSD and resolve shear stress influence the strain localization and crack initiation behaviors. The distribution of a localization parameter calculated based on the multiplication of FSD and Schmid factor within a grain is found to correlate well with the locations of PSBs. The maximum values of the localization parameters within a microstructure are shown to correlate well with the experimentally obtained crack initiation lives. The presence of volumetric defects in IN-718 generally do not impact strain localization behavior unless their size is large compared to the grain size.

1. Introduction

Additive manufacturing (AM), such as laser (beam) powder bed fusion (L-PBF or LB-PBF), fabricates parts in a layer-by-layer fashion and offers significant benefits over conventional manufacturing such as near net shaping and consolidating assemblies into monolithic parts [1,2]. It therefore has strong potential to be adopted for the fabrication of hard-to-machine alloys such as Ti alloys and Ni-base superalloys, which are often used for the fabrication of complex parts in load-bearing applications [3-5]. However, additively manufactured (AMed) parts typically contain large population of volumetric defects which act as stress risers and can be detrimental to the mechanical properties especially their fatigue behavior. Fatigue fracture of many AMed metallic materials in

the mid and high cycle fatigue (MCF and HCF) regimes often is dominated by the volumetric defects, such as lack-of-fusions, gas entrapped pores, and keyholes, which can accelerate the initiation of fatigue cracks, introduce uncertainty to and deteriorate the fatigue performance [6,7]. In general, an inverse correlation between defect size and fatigue resistance exists for most AM materials [8,9].

Inconel 718 (IN-718) is perhaps one of the most popular Ni-base superalloy for various AM technologies owing to its excellent weldability [10]. Interestingly, this material does not appear to be as sensitive to the presence of defects as other alloys, e.g., Ti-6Al-4 V and 17–4 precipitation hardening stainless steel [11,12]. In fact, in the machined surface condition, volumetric defects are not always responsible for the initiation of the main fatigue crack for AMed IN-718 [13-15]. For LB-PBF IN-718, Wan et al. [16] reported that the process induced gas-entrapped

---

Nomenclature

a	Stress exponent for phenomenological crystal plasticity model	t	Schmid factor exponent
d	Average grain size	u	Hardening Coefficient
F	Deformation gradient	α	Slip system
F^e	Elastic deformation gradient	β	Slip plane designator
F^p	Plastic deformation gradient	ε_{max}	Maximum strain amplitude
h_0	Initial hardening parameter	ε_{min}	Minimum strain amplitude
$h_{\alpha\alpha'}$	Hardening matrix	η	Square root of the area of a slip plane surrounded by grain boundary
J_2	Second invariant of stress tensor	σ	Fatigue limit
k	Hall Petch constant	σ_0	Hall Petch constant
L	Velocity gradient	$\dot{\gamma}_\alpha$	Rate of shear for slip system α
L^e	Elastic Velocity gradient	$\dot{\gamma}_0$	Reference shear rate on slip system α
L^p	Plastic velocity gradient	τ_α	Resolved shear stress on slip system α
l	Free slip distance exponent	χ_α	Back stress on slip system α
m_α	Unit vector normal to the slip plane	ξ_α	Critical resolved shear stress on slip system α
m	Strain rate sensitivity	$\dot{\chi}_\alpha$	Rate of change of back stress on Slip system α
M_p	Mandel stress tensor	ξ_α^{ini}	Initial critical resolved shear stress
M_p^{dev}	Deviatoric Mandel stress tensor	$\xi_{\alpha_0}^{ini}$	Reference initial critical resolved shear stress
$\|M_p^{dev}\|_F$	Frobenius norm of the deviatoric Mandel stress	ξ_α^{sat}	Saturation critical resolved shear stress
N_s	Number of slip systems	$\xi_{\alpha_0}^{sat}$	Reference saturation critical resolved shear stress
q	Stress exponent for Isotropic plastic material model	λ	Free slip distance threshold
r	Dynamic recovery coefficient	ω	Scalar resistance to plastic flow
R_ε	Strain ratio	ω^{sat}	Saturation resistance
s_α	Unit vector parallel to the slip direction	δ	Localization parameter
T	Taylor factor	θ	Average Schmid factor for all slip systems on a slip plane

pores always served as the initiation sites for the main fatigue cracks in the MCF and HCF regimes; however, Yang et al. [17] observed that in HCF and very high cycle fatigue (VHCF) regimes crack initiation can be either from volumetric defects or from crystallographic facets, despite that the critical defects from both works were mostly spherical and were ~20 μm in diameter. Recently, Muhammad et al. reported that, irrespective of the test frequency of 5 Hz or 20 kHz, fatigue crack initiation almost exclusively occured from crystallographic facets in HCF and VHCF regimes, even though the maximum defect diameter was ~40 μm [13]. These observations from the literature suggested that the defect- and facet- driven fatigue crack initiation mechanisms in the LB-PBF IN-718 may be competing. However, the factors governing this competition are not solely related to the defect size and are presently not well known.

The crystallographic facets serving as the initiation sites suggests the initiation of fatigue cracks may be ascribed to the persistent slip bands (PSBs) which form along slip planes [18]. Under cyclic loading, the operation of PSBs not only form intrusions/extrusions at free surfaces and internal microstructural discontinuities, such as grain boundaries (GBs) or secondary phases, but also generate vacancies within the bands due to the climb/annihilation of edge dislocations [19,20]. The former creates the driving force for crack formation, while the latter provides a pathway for the short crack growth in the "damaged material"– which is the typical planar feature often seen on the crack initiation sites [21]. The extent (depth or height) of the intrusions/extrusions formed, therefore the driving force for crack formation, is directly proportional to the size (in-plane dimension) of the PSBs [22]. In addition, a longer free slip distance (FSD) between adjacent microstructural discontinuities favors the formation of the PSBs. Therefore, fatigue crack initiation via PSBs is easier with larger FSD, and vice versa. The competition between the defect- and the PSB- driven crack initiation mechanisms can be hypothesized to be governed by the relative size of the defects and FSD.

This hypothesis appears to be consistent with the observations reported in the literature. In fact, Yang et al. showed that on the fracture surfaces where both initiation mechanisms were evident, the size of the facets were quite comparable with that of the volumetric defects – around 20 μm in diameter [17]. In contrast, the facet size reported by Muhammad et al. was well above 100 μm in diameter, which was significantly larger than the diameter of the largest defects observed via X-ray CT (~40 μm). In this case, the crack initiation via PSB was perhaps easier. This was further confirmed by their observations that the diagonally built specimens exhibited larger facets at crack initiation sites and weaker fatigue resistance compared to the vertically built specimens. On the other hand, the IN-718 microstructure reported by Wan et al., where no PSB governed crack initiation was observed, contained closely spaced δ phase (several microns or smaller in distance), which limited the FSD, and thus, inhibited the formation of PSBs [16].

This work aims to discover the factors governing the competing fatigue crack initiation mechanisms, i.e., PSB- vs. defect- mediated, in AMed IN-718 via crystal plasticity (CP) simulations validated by experiments. To capture the cyclic strain localization as well as the crack initiation behaviors of IN-718, a physics-based CP slip strength evolution law and a crack initiation criterion are proposed and implemented in the CP simulations. The influence of the presence of volumetric defects of varying size on the formation of PSBs and fatigue cracks are also investigated using the simulations. The hypothesized governance of the relative size between defects and FSD on the crack initiating mechanisms is confirmed by simulation. Experimentally, fully-reversed uniaxial fatigue tests are performed in strain-controlled mode on machined LB-PBF IN-718 specimens undergone two heat treatment schedules to induce both fine and coarse microstructures for assessing the influence of FSD on the fatigue crack initiation resistance. With the selective application of hot isostatic pressing (HIP), the fine and coarse microstructures will respectively contain large and small defects, which generates a broad range of relative size between defects and FSD.

This manuscript is organized as the following: Section 2 provides a brief overview on the physical aspects of cyclic strain localization, PSB formation, and crack initiation; Section 3 describes methodology, which

include the CP framework used, setup of the model geometry, and experimental procedure; results of the simulations along with the experimental observations are provided and discussed in Section 4; finally, conclusions are drawn in Section 5.

2. Physics of fatigue crack initiation

Under cyclic loading, metallic materials undergo permanent microstructural changes as the loading continues which eventually lead to initiation of fatigue cracks. The propagation of the major crack(s) is generally responsible for the fatigue failure of an engineering component. In the initial loading stage, dislocations in single-phase metals (including pure Cu, Ni and Ag, as well as solid solution alloys such as austenitic stainless steels, IN625 and Hastelloy X) typically significantly multiply—leading to increase in overall dislocation density—and rearrange into relatively low energy configurations such as bundles of edge dislocation dipoles and multipoles [23-26]. This is typically accompanied by a relatively rapid cyclic hardening. With presence of dislocation bundles, deformation is typically carried out by the screw dislocations connecting neighboring bundles. Continued cyclic deformation from this stage can cause the collapse of the bundles into dislocation walls with higher dislocation density within narrow regions (i.e., PSBs) along a favorable slip plane [27,28]. The spacing between walls is significantly larger than that between bundles which favors the slip within the PSBs [19,29-32]. The contrast in slip resistance between the cyclically hardened grains and the softened PSBs essentially localizes the slip activities within the latter. In fact, two orders of magnitude higher strains have been measured in PSBs as compared to the grains [33,34].

In precipitation hardened alloys (such as the γ' and γ'' hardened Ni-base superalloys), the to-and-fro motion of screw dislocations within the PSBs can shear the precipitates (see depictions in Fig. 1). Since the motion of screw dislocations is irreversible due to cross-slip events, the repetitive and irreversible shearing of precipitates can induce mechanical dissolution of the precipitates in the PSBs. The shearing of precipitates within the PSBs further facilitates slip in the PSBs, increases the contrast in slip resistance between the PSBs and the matrix, and provides a more favorable condition for strain localization within the PSBs [35,36].

PSBs forms along slip planes but cannot penetrate strong obstacles that are opaque to dislocation glide, such as twin boundaries, GBs, and non-shearable particles. As a result, they are typically confined between neighboring obstacles. In a single-phase alloy, PSBs generally extend fully within the grains along the slip planes where the grain's cross sections are the largest and the PSBs size essentially equates the grain size. In addition, these obstacles can impose strong back stress on PSBs [37] making their formation/operation stress dependent on the free slip distance between the obstacles, i.e., smaller distances make the formation/operation more difficult requiring higher stress amplitudes. For instance, it has been shown that in single-phase FCC materials such as brass, pure Cu, and pure Al the PSBs form on the largest cross sections of grains and the fatigue limits are inversely related to the grain size following a Hall-Petch like relation [38], i.e.,

$$\sigma = \sigma_0 + k/\sqrt{d} \qquad (1)$$

where σ is the fatigue limit, d is the average grain size or the average free slip distance within the grains, and σ_0 and k are constants. It follows that the difficulty of forming PSBs is not constant within the material given the natural variation in grain size with larger grains favorable for PSBs to form [39,40]. In fact, this difficulty is not constant even within the same grain, since the dislocations free slip distance (FSD) is location dependent; i.e., formation of PSBs is easier at locations where the free slip distance is longer. In smaller grains, the absolute difference of FSD among parallel slip systems or among different slip systems is inherently small compared to larger grains. As a result (excluding the scenarios of ultrafine grained materials for which the dislocation densities are very low due to dislocation starvation), the contrast in slip resistance among different slip systems tends to be small, giving rise to multiple slip systems being active and dislocation configuration being homogeneous compared to the formation of cells and walls in larger grains [41]. This suggests that one favorable condition for the formation of PSBs may be "the existence of a slip system with the advantage of easy glide over other systems, dictated by grain orientation and/or size".

In metallic materials where defect population and size are relatively small, fatigue cracks typically initiates along PSBs due to their interaction with either free surfaces or GBs [33,34,42-45]. When intersected with free surfaces, PSBs form persistent slip markings (or intrusions and extrusions) on the surface [46-48]. When intersected with GBs, they induce stress concentrations at these locations. Both scenarios favor the initiation of transgranular cracks. The path along which the microstructurally small cracks form typically does not follow precisely the center line of the PSBs; instead, it coincides with the PSB-matrix interface where the normal-to-PSB gradient in the cyclic plastic shear strain is the maximum. Although the slip activities within an individual PSB are not completely uniform through the thickness of PSBs, the magnitude of such variations are generally small [49]. The driving force for fatigue
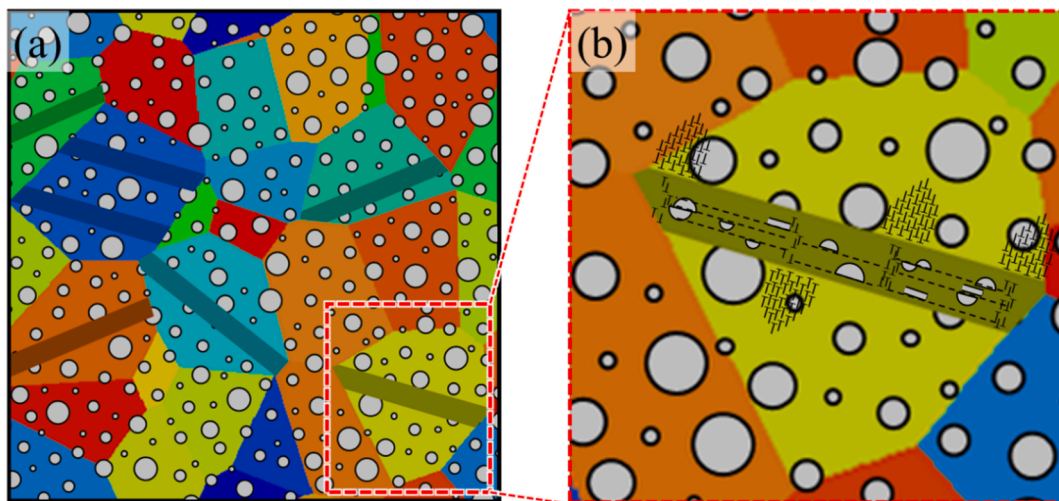

Fig. 1. Schematic illustration of the presence of PSBs in a polycrystalline material with shearable precipitates. Colored patches represent different grains. Dark colored bands represent PSBs. Gray circles represent precipitates. A magnified view of a grain in (a) is shown in (b) where the presence of dislocation bundles and dislocation-precipitate interactions are depicted.

crack initiation from PSBs is directly proportional to the magnitude of the extrusions which, in turn, is correlated to the grain size and the slip irreversibility within the PSBs [21]. Specifically, the larger the grain size and/or the higher the degree of slip irreversibility, the higher the extrusion amplitude. The slip reversibility is influenced by the intrinsic material properties such as extended fault energies (including the stacking fault energy (SFE) in an FCC matrix or antiphase boundary energy (APBE) in the ordered precipitates); i.e., higher fault energies cause wavier slip, wider PSBs, and less slip reversibility, and vice versa [33].

With the presence of defects relatively large compared to their surrounding grains, the associated stress concentrations can cause localized plastic deformation in its vicinity which may accelerate the formation of PSBs, inducing defect- mediated fatigue crack initiation [50]. On the other hand, if the defects are significantly smaller compared to surrounding grains, the material volume that experiences the elevated stresses may not be sufficient to achieve this acceleration; and fatigue crack initiation is expected to be slip induced and transgranular. Determining the precise conditions that favor the one mechanism over the other by means of pure experimentation is challenging as the required direct observations on crack initiation are often hindered by the subsurface nature of critical volumetric defects. An ideal supplementation to experiments would be a physics-based numerical model that can simulate the microstructural evolution in AMed metallic materials from the onset of cyclic loading up to the initiation of fatigue cracks. Among others, CP modeling, including the finite element based, phase field based, and spectral solver based ones, can explicitly model the deformation of grain aggregates (with or without volumetric defects) and, if the back stress term is implemented, their cyclic response [50-60]. If proper fatigue indicator parameters are incorporated, the initiation of fatigue cracks can also be modeled [61-64]. Nevertheless, appropriate material strength and hardening kinetics models are needed in order to adequately capture the location dependent slip resistance and its evolution under cyclic loading that leads to the eventual formation of PSBs and initiation of fatigue cracks.

3. Methodology

This work proposes an FSD-based material strength model compatible with the CP framework and suitable to model the cyclic response of IN-718. Spectral solver based CP simulations with this strength model implemented are performed using Düsseldorf Advanced Material Simulation Kit (DAMASK) to understand the competitive mechanisms of fatigue crack initiation from AM volumetric defects or PSBs in AM IN-718 [65]. To validate the simulation results, fatigue performance of LB-PBF IN-718 specimens, heat treated to result in both coarse and fine microstructures, were evaluated using strain-controlled fatigue tests. This section details the CP framework implemented as well as the numerical and experimental procedures carried out.

3.1. Crystal plasticity formulation

CP multiplicably decomposes the total deformation gradient (F) into elastic and plastic parts, i.e., $F = F^e F^p$. Accordingly, the velocity gradient ($L = \dot{F} F^{-1}$) can be additively decomposed into elastic and plastic parts, i.e., $L = L^e + F^e L^p F^{e-1}$. The plastic velocity gradient (L^p) was described in this work via two different material models depending on the regions of interest. Specifically, phenomenological CP was applied for the IN-718 crystallites within the model and —since the spectral solver based CP does not explicitly model free surfaces— isotropic plasticity with very low material strengths was applied to mimic the behavior of volumetric defects (pores).

In the framework of CP (applied for IN-718 crystallites), the plastic velocity gradient (L^p) is calculated as the summation of shear rates contributed by each slip system α, i.e.:

$$L^p = \sum_{\alpha=1}^{N_s} \dot{\gamma}_\alpha (s_\alpha \otimes m_\alpha) \tag{2}$$

where s_α and m_α are the unit vectors parallel to the slip direction and normal to the slip plane—their dyadic product ($s_\alpha \otimes m_\alpha$) is also called the Schmid tensor, $\dot{\gamma}_\alpha$ is the corresponding shear rate, and N_s is the number of slip systems. The shear rate ($\dot{\gamma}_\alpha$) given by the following flow rule is used for IN-718:

$$\dot{\gamma}_\alpha = \dot{\gamma}_0 \left| \frac{\tau_\alpha - \chi_\alpha}{\xi_\alpha} \right|^{1/m} \mathrm{sgn}(\tau_\alpha - \chi_\alpha) \tag{3}$$

where $\dot{\gamma}_0$ is the reference rate of the shear strain, τ_α is the resolved shear stress, χ_α is the back stress, ξ_α is the slip resistance on slip system α, and m is the strain rate sensitivity. The back stress is a long-range stress exerted by dislocations previously deposited onto barriers (such as dislocation bundles and walls) to repel the motion of the new gliding dislocations. Back stress generated from the forward loading direction can significantly reduce the yield point in the reverse loading direction and is believed to be the cause of Bauschinger effect. Back stress also evolves during cyclic loading whose rate, in this work, is described by the Armstrong and Frederick (AF) model [66] using the rate of plastic strain:

$$\dot{\chi}_\alpha = u\dot{\gamma}_\alpha - r\chi_\alpha \left| \dot{\gamma}_\alpha \right| \tag{4}$$

where u is the hardening coefficient and r is the dynamic recovery parameter.

Conventionally, the evolution rate of critical resolved shear stress (or slip resistance) in a slip system is attributed to the shear strain in all active slip systems [65] by:

$$\dot{\xi}_\alpha = \sum_{\alpha'=1}^{N_s} h_{\alpha\alpha'} \left| \dot{\gamma}_{\alpha'} \right| \left| 1 - \frac{\xi_{\alpha'}}{\xi_{\alpha'}^{sat}} \right|^a \mathrm{sgn}\left(1 - \frac{\xi_{\alpha'}}{\xi_{\alpha'}^{sat}} \right) \tag{5}$$

where $h_{\alpha\alpha'}$ is the hardening matrix that empirically considers the self (dislocation-dislocation interaction within the same slip system, i.e., when $\alpha = \alpha'$) and latent (dislocation-dislocation interaction between slip systems, i.e., when $\alpha \neq \alpha'$) hardenings; and ξ_α^{sat} is the saturation value of the slip resistance on system α. The initial and saturation values of slip resistance (ξ_α^{ini} and ξ_α^{sat}) of a material point are dependent on its FSD by a Hall-Petch law. Specifically, the FSD parameter (η_α) is defined as the $\sqrt{area}$ of the slip planes within a grain. Fig. 2 illustrates the procedure to calculate η_α: for each slip plane, the grain was first sectioned into slabs of equal thickness ($t = 2$ voxels was used in this study) and the area of slab i was calculated based on the number of voxels contained. Accordingly, although for each material point (or voxel) the FSD parameter is calculated for each slip system, the η_α values of slip systems that belong to the same planes are the same. Based on the defined FSD parameter, the initial and final slip resistances are expressed as:

$$\xi_\alpha^{ini} = \xi_\alpha^{ini_0} + k/\sqrt{\eta_\alpha}, \xi_\alpha^{sat} = \xi_\alpha^{sat_0} + k/\sqrt{\eta_\alpha} \tag{6}$$

where k is the Hall-Petch parameter, ξ_α^{ini} and ξ_α^{sat} are the initial/saturation slip resistances on system α, and $\xi_\alpha^{ini_0}$ and $\xi_\alpha^{sat_0}$ are the reference initial/saturation slip resistances. A lower saturation strength than the initial strength indicates cyclic softening, and vice versa. Replacing Eq. (5), the location-dependent evolution rate of the slip resistance can be calculated based on:

$$\dot{\xi}_\alpha = \sum_{\alpha'=1}^{N_s} h_{\alpha\alpha'} \left| \dot{\gamma}_{\alpha'} \right| \left| 1 - \frac{\xi_{\alpha'}}{\xi_{\alpha'}^{sat}} \right|^a \mathrm{sgn}\left(1 - \frac{\xi_{\alpha'}}{\xi_{\alpha'}^{sat}} \right) \mathrm{sgn}(\eta_\alpha - \lambda) \tag{7}$$

where λ is the FSD threshold parameter. As discussed in Section 2, depending on the FSD, certain regions of a grain may experience local cyclic hardening (when FSD is small) due to the formation of dislocation
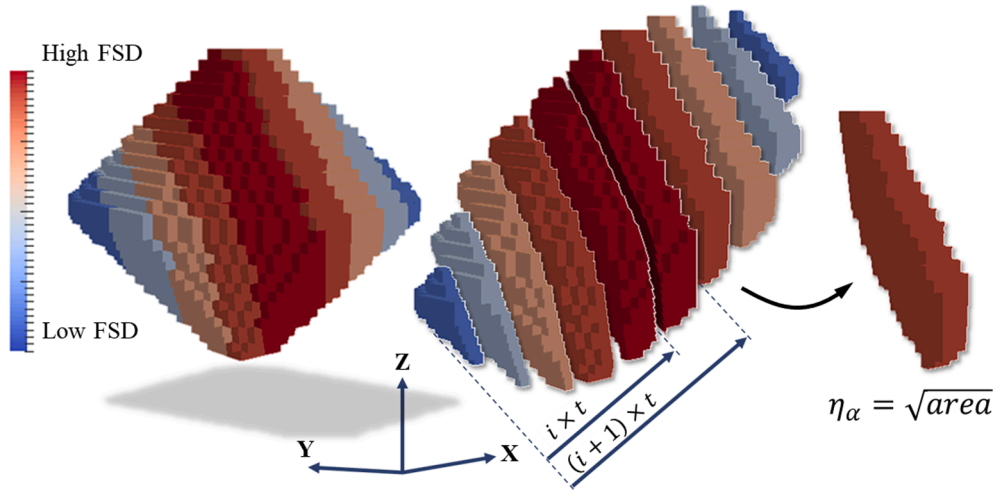
Fig. 2. Schematic illustration of the calculation and assignment procedure of FSD.

bundles while others soften when the bundles collapse into PSBs (when FSD is large). The threshold FSD value governing the hardening/softening behavior is specified in this work as λ, which may vary depending on the slip characteristics of a material, i.e., planar or wavy slip, dictated by its planar fault energies (such as SFE and APBE) [27,67,68]. Such information can be calculated from a lower length scale, such as using atomistic simulations, passed onto crystal plasticity in a multiscale framework [69].

The velocity gradient of the pores in the grain aggregate is described by isotropic elasto-plastic material model as it has been implemented within DAMASK:

$$L_p = \frac{\dot{\gamma}_p}{T} \frac{M_p^{dev}}{\|M_p^{dev}\|_F} \tag{8}$$

where $\dot{\gamma}_p$ is the rate of plastic shear strain, M_p^{dev} is the deviatoric Mandel stress tensor, T is the Taylor factor, and $\|M_p^{dev}\|_F$ is the Frobenius norm of the deviatoric Mandel stress. The rate of shear in the material is defined by:

$$\dot{\gamma}_p = \dot{\gamma}_0 \left(\frac{\sqrt{3J_2}}{T\omega} \right)^q \tag{9}$$

where J_2 is the second invariant of the Mandel stress tensor (M_p), q is the stress exponent, and ω denotes the scalar resistance to plastic flow. The evolution of the resistance parameter (ω) is defined by:

$$\dot{\omega} = \dot{\gamma} h_0 \left| 1 - \frac{\omega}{\omega^{sat}} \right|^a \text{sgn}\left(1 - \frac{\omega}{\omega^{sat}} \right) \tag{10}$$

where h_0 is the initial hardening parameter, ω^{sat} the saturation resistance, and a is the strain rate sensitivity exponent.

To obtain the material parameters for the CP model (Eqs. (1)–(10)), virtual single crystal simulations were performed to fit the obtained material response under both tensile and cyclic loadings to experimentally measured curves (the experimental procedure was provided in Section 3.3). For these simulations, elastic constants identical to what have been used in the literature for IN-718 were used [70,71] (See Table 1). This virtual single crystal simulations perform both uniaxial

tensile and fully-reversed cyclic loadings 50 times on single crystals with random orientations. Under the eigen-strain Taylor assumption, the average stress-strain curves from the simulations, which were assumed to represent the polycrystalline response, were then fitted to the experimental ones. The procedure for virtual single crystal tensile simulations were detailed elsewhere [37,72-74]. The simulated responses in the first cycle from unloaded condition to the maximum strain were fitted to the experimental tensile test results. For calibrations with cyclic loading, several strain amplitudes of 0.006, 0.008, and 0.010 mm/mm were applied for 250 cycles, and the saturated cyclic stress-strain responses were fitted to experimental data with corresponding strain amplitudes. The tensile stress-strain curves and cyclic hysteresis loops for all strain amplitudes, overlaid with experimental data, are presented in Fig. 3. The material parameters obtained as the result of fitting procedure are listed in Table 1.

3.2. Model geometries

A fast Fourier transform-based method, also referred to as the spectral method, implemented in the DAMASK, was used to perform the CP simulations [65]. The spectral method implicitly assumes periodic boundary conditions along X, Y, and Z directions. The computational cells contained grain aggregates that form a representative volume element (RVE) of the material discretized by a 33 (X) × 33 (Y) × 32 (Z) grid system. The physical length of the cubic RVEs on each side was 115 μm. A polycrystalline aggregate containing 23 small grains surrounding a large grain was generated by modifying a Voronoi tessellated grain structure with relatively uniform grain sizes. This type of synthesized geometry on one hand replicated the presence of both very large and very small grains in the LB-PBF IN-718 microstructure [13,75-77]; on the other hand, the large grain contained sufficient integration points which permitted analysis of transgranular strain distribution. The cutaway views of the modelled geometries are provided in Fig. 4. A defect-free microstructure and one containing a pore are shown in Fig. 4 (a-b), respectively.

To assess the effect of grain orientation on the strain localization, the orientation of the central grain is systematically varied. Inverse pole figure (IPF) maps of post heat treatment microstructure of IN-718

Table 1
Material constants used in the CP simulations for IN-718 crystallites: elastic constants adopted from the literature ([65,66]) and plastic constants obtained by fitting materials response from virtual single crystal simulations to experiments.

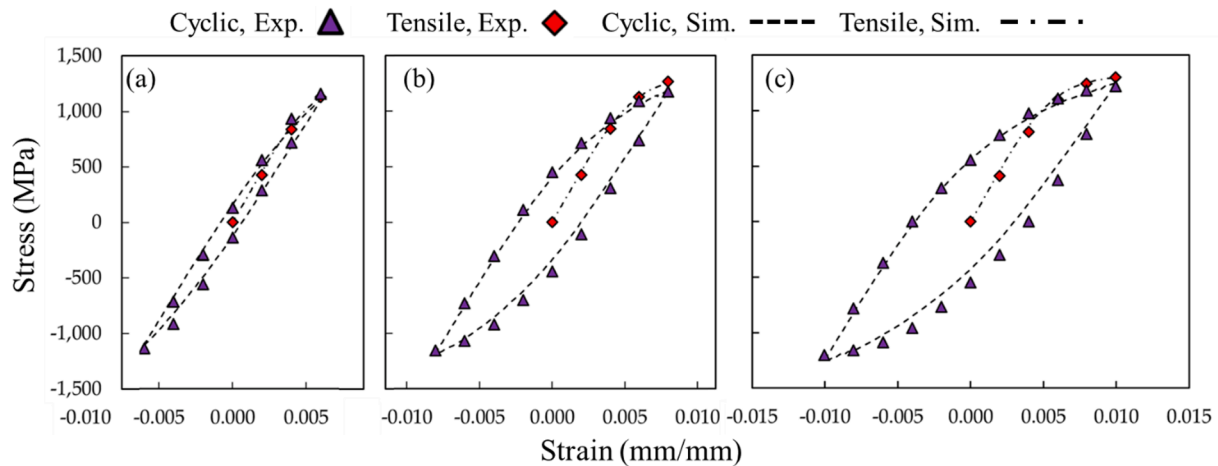| C_{11}(GPa)	C_{12}(GPa)	C_{44}(GPa)	$\dot{\gamma}_0$(s^{-1})	m	u(MPa)	r	$\dot{\chi}_0$(MPa·s^{-1})	$\xi_\alpha^{ini_0}$(MPa)	$\xi_\alpha^{sat_0}$(MPa)	a	h_0^{s-s}	k (MPa)	λ (μm)
259.6	179.0	109.6	0.007	0.13	39.0	0.4	10.0	300.0	100.0	1.0	100.0	0.4	40.0

Fig. 3. Monotonic and cyclic responses obtained from virtual single crystal simulations fitted to experimental data at different strain amplitudes of (a) 0.006, (b) 0.008 and (c) 0.010 mm/mm.
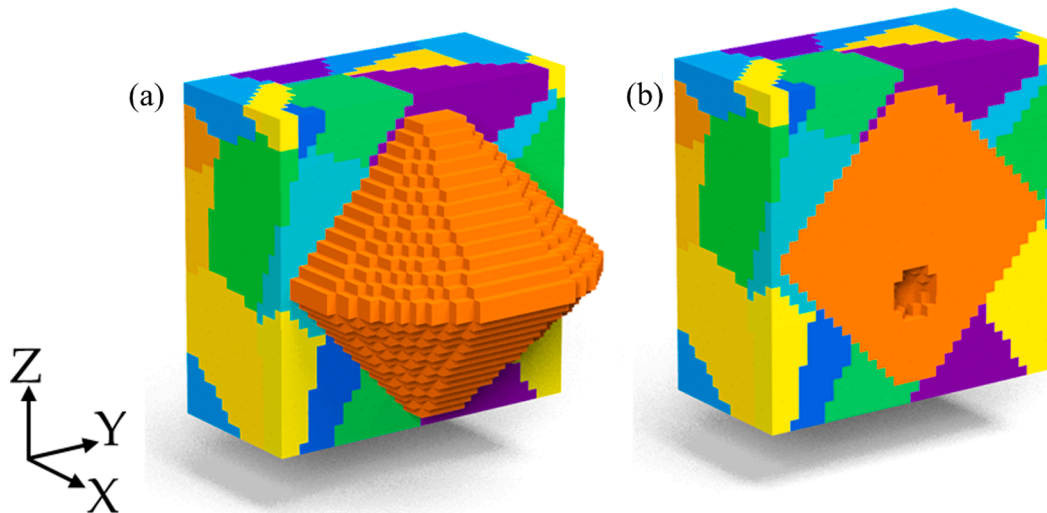

Fig. 4. Representative volume elements containing a polycrystalline aggregate of 24 grains used to simulate: (a) pristine and (b) defective grain structure.

considered in this study do not show a particular texture along the build direction (see Fig. 5(a & d) or the transverse direction (see Fig. 5(b & e)). Grain size distributions of LB-PBF IN-718 specimens in both radial and transverse planes are shown in Fig. 6 as well. The distributions corroborated with the presence of both very large and very small grains visible in Fig. 5, which was modeled in this work. Detailed experimental procedure used to obtain such data is given in Section 3.3. As such, three main crystallographic poles of the central grain; i.e., [100], [101], and [111], were chosen to align with Z axis (as schematically illustrated by Fig. 7(a-c). If the loading is along the Z direction, the three pole alignments should produce three constant maximum Schmid factors, irrespective of any rotation of the crystallographic coordinate about Z axis. To further diversify the range of Schmid factors probed, a diagonal loading direction, i.e., along line X = −Z and Y = 0, was also applied.

When the loading direction is diagonal, for each pole orientation along Z, relatively large variations in the maximum Schmid factor are achieved by rotating the crystal coordinates about Z. The maximum values of the Schmid factor (θ) among all slip systems with respect to rotation about Z axis are plotted for both loading directions in Fig. 7(d-f) (corresponding to the Z axis orientations presented in Fig. 7(a-c). Note that due to the periodicity only the Schmid factors for a 180° rotation are plotted. As indicated by red square markers, a few points with different Schmid factors are chosen and the corresponding orientation is assigned

to the grain of interest in the RVE. A complete list of the defect-free RVEs modeled in this study is presented in Table 2.

Multiple cases of the RVE containing a pore with different sizes were modeled. A schematic representation of the RVE including a pore is provided in Fig. 4(b). These RVE models were based on Case No. 14 shown in Table 2, where the [111] pole of the central grain aligns with Z axis, and the loading direction is diagonal. The location of the pore remained constant for all cases. Three different pore diameters ranging between 3.5 and 17.5 μm were considered. The defect statistics in the two microstructures as measured from both XCT and 2D optical analysis are shown in Fig. 8(a & b). The experimental procedures used to obtain such data is provided in Section 3.3. The modeled defect size range appeared to be realistic as the largest defects revealed by X-ray computed tomography (XCT) scans performed on the small coupons extracted from the specimens in this study were in the range of 15–20 μm (Fig. 8(a)). It is also notable that the XCT analysis did not reveal any defects in the coarse microstructure within the small volume sampled, which is likely due to the different heat treatment applied (to be elaborated in Section 3.3). 2D optical analysis sampled larger volume and have detected some small defects in the coarse microstructure (Fig. 8 (b)).

To mimic the mechanical behavior of pores, the material constants should ideally be chosen so that both the elastic constants and strength
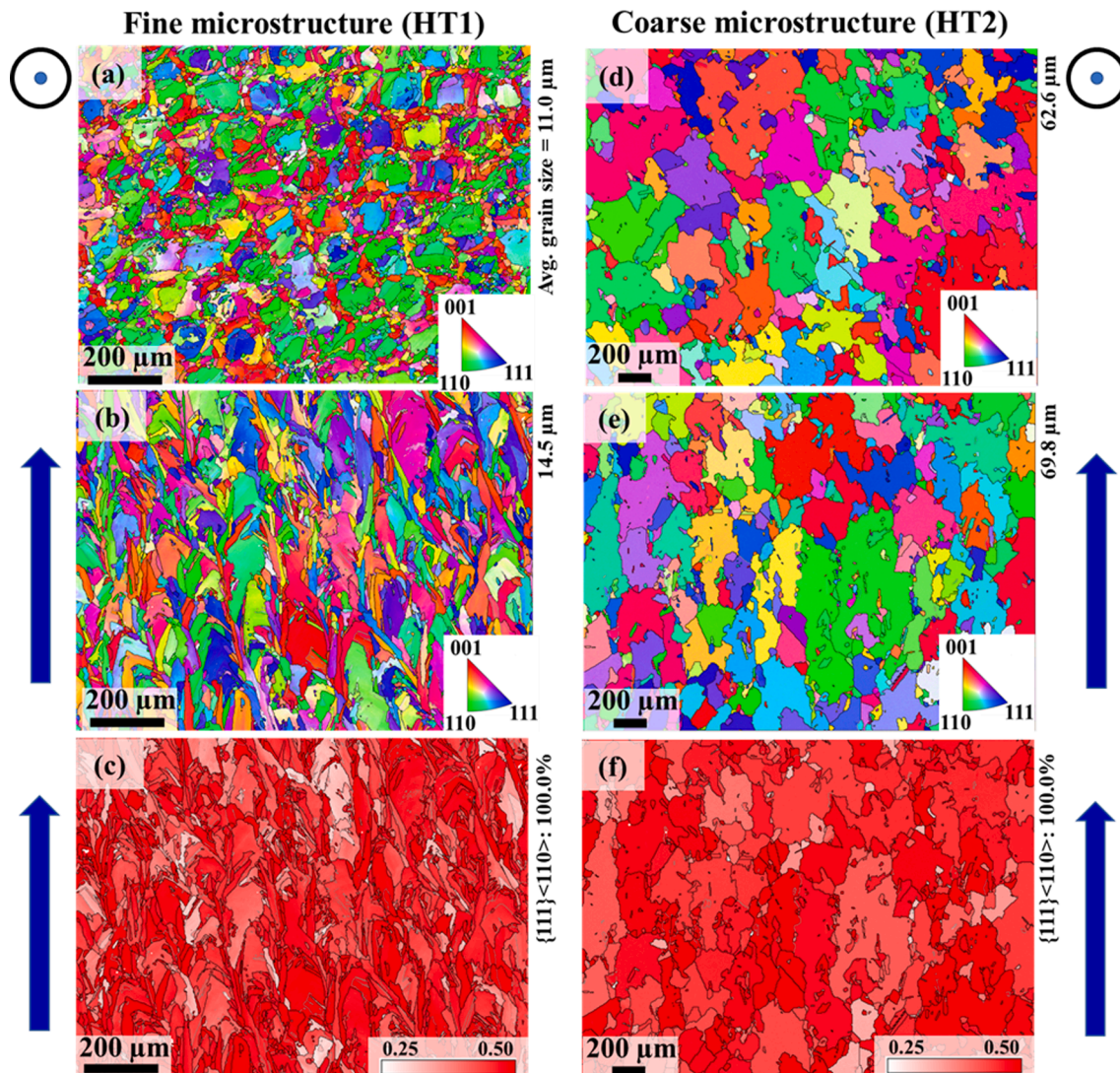
Fig. 5. IPF maps showing the microstructures of IN-718 specimens heat treated to result in fine ((a) radial and (b) transverse planes) and coarse ((d) radial and (e) transverse planes) microstructures. Material points are colored according to the normal directions of the respective planes. Arrows indicate the build orientations. Schmid factor maps at transverse planes for (c) fine and (f) coarse microstructure assuming the loading is along the build directions.

are significantly lower than the ones for IN-718. Maiti et al. suggested one order of magnitude lower elastic constants for the buffer layer to model free surface and void (similar to Set 2 parameters in Table 3) [78] which were effective under monotonic loading. However, in this work performed simulations of cyclic loading and applying these parameters resulted in numerical convergence issues due to the rapid softening in certain integration points. To circumvent these numerical issues encountered during cyclic loading, a material with similar elastic constants to the ones that had been used for the IN-718 and significantly lower yield strength were applied to the pores (i.e., Set 1 parameters in Table 3). To verify the soundness of the chosen material constants, simple tension simulations of the microstructure containing a pore were performed while the IN-718 matrix was treated as linear elastic solids. Two different sets of material parameters as listed in Table 3 were assigned to the pore region and the stress responses near the pores were compared. Fig. 9 visualizes the von Mises stress solutions along the dashed arrow passing through the pore for both cases. The relative difference in the stress solutions versus location is also plotted on the same graph. Only a maximum of ~6 percent difference in the stress response is noticed across the two cases.

Uniaxial fully-reversed cyclic loading with constant, 0.012 mm/mm, strain amplitude was simulated for 250 cycles for all cases. Note that,

although the simulated cycles appeared to be a small number compared to the actual cycles required for nucleation and early growth of short cracks (which is typically over thousands of cycles), the former when scaled (i.e., each simulated cycle representing a few tens or hundreds of experimental cycles) were shown to correlate well with the latter [58,79]. Upon conclusion of the simulations, the material response was post processed and analyzed to investigate strain localization and crack initiation behaviors.

3.3. Experimental procedures

The near-net shape fatigue specimens used in this study were fabricated using gas atomized IN-718 powder in an argon purged environment via the LB-PBF process utilizing an EOS M290 AM system and manufacturer recommended process parameters, as listed in Table 4. Fatigue specimens were designed and machined according to ASTM E606 (see Fig. 10) [80]. The machining process was turning only, which was identical to the turning process used by Lee et al. [81]. This process resulted in surface roughness values of $R_a = 0.77$ μm, $R_p = 2.34$ μm, and $R_v = 2.40$ μm.

Two different HT procedures, as listed in Table 5, were applied to the LB-PBF IN-718 specimens prior to machining (details regarding HT1 are
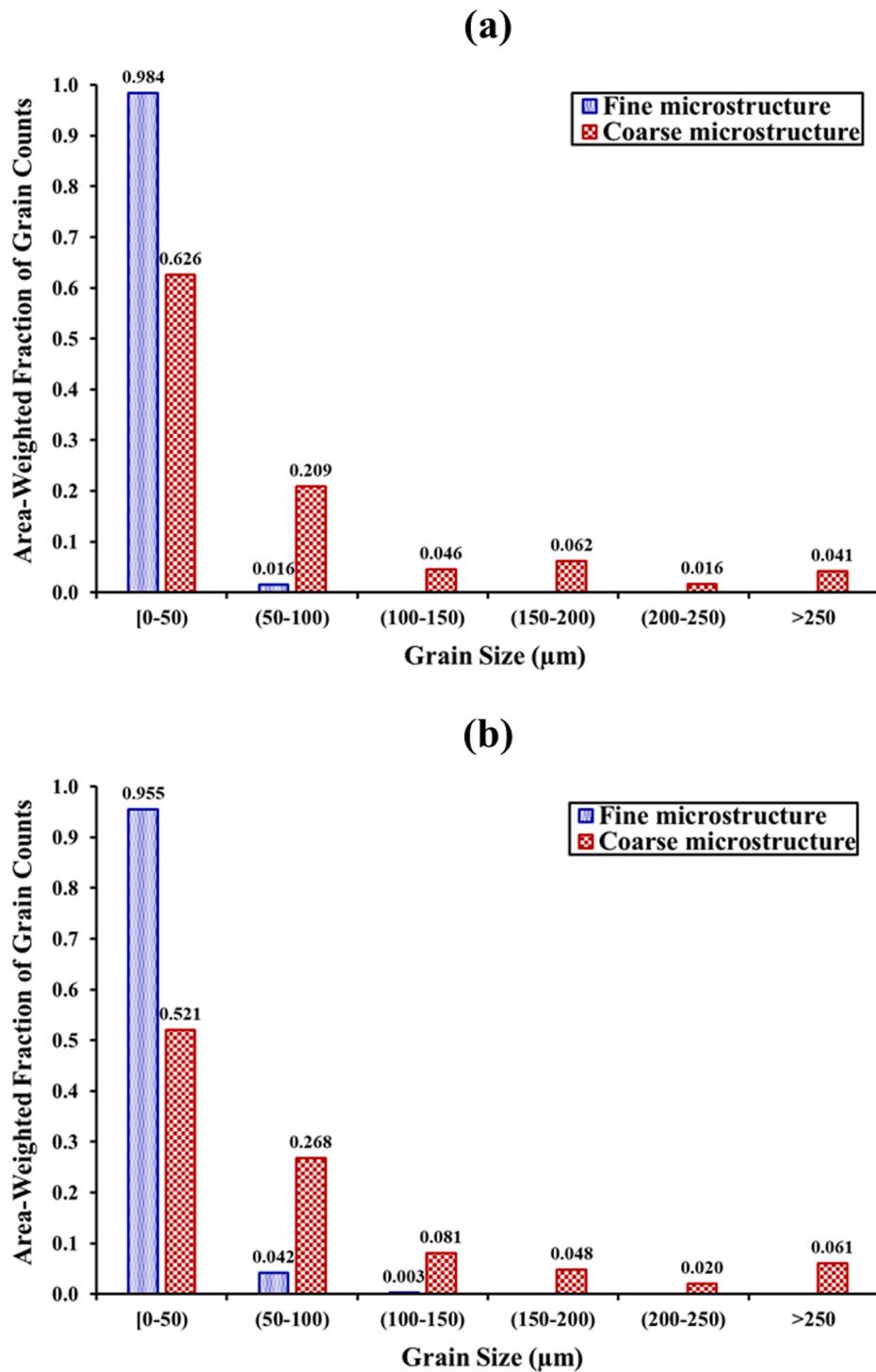
(a)

(b)

Fig. 6. Grain size distribution for fine and coarse microstructure of LB-PBF Inconel 718 in (a) radial and (b) transverse planes.

obtained from Lee et al. [81]). All the heat treatments were conducted in an electric furnace in an argon environment. All specimens were stress-relieved at 1066 °C for 1.5 h according to the ASTM F3055-14a standard prior to removing them from the build platform [82]. Following stress-relieving, the fatigue test specimens went through an optional HIP step (only HT2 went through HIP), solution treatment, and double aging according to ASTM F3055-14a and AMS 2774 standards [82,83]. As shown in Fig. 5, the HT2 induced a much coarser microstructure compared to HT1, which likely was due to the additional exposure to 1163 °C for 3 h.

A Zeiss Crossbeam 550 SEM with electron backscatter diffraction

(EBSD) and backscattered electron detectors was utilized for micro-structural analysis. The microstructure of IN-718 specimens in this study was investigated using EBSD analysis and electron channeling contrast imaging (ECCI). For microstructure analysis, HT1 and HT2 samples were cut and mounted in planes both parallel and perpendicular to the build direction and polished to mirror surface finish according to the ASTM E3 standard [84]. Initially, the samples were ground and polished using sandpapers up to 1200 grits and then polished using polishing pads until mirror finish. In addition, a vibratory polisher was employed for 5 h to ensure removal of any remaining minor surface scratches from previous polishing steps.
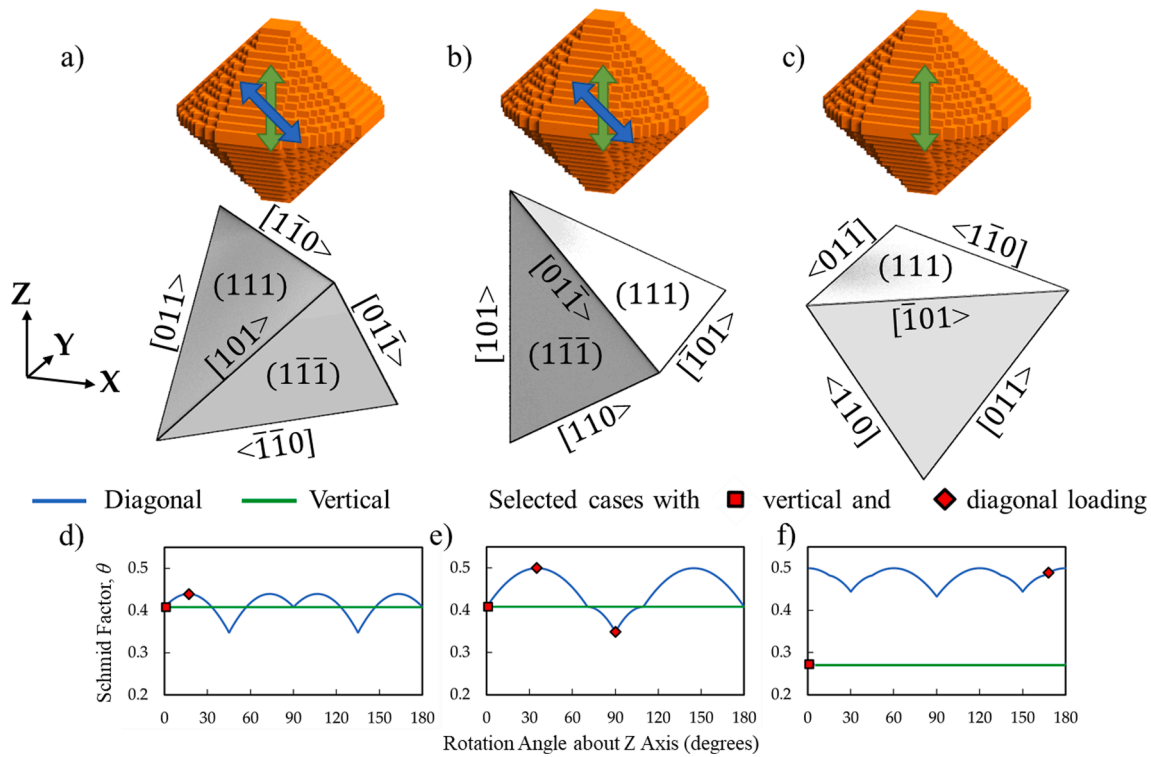
Fig. 7. Schematic illustrations of orientations of the central grain using Thompson's tetrahedra with respect to the vertical (green arrows) and diagonal (blue arrow) loading directions: (a) Z//[100], (b) Z//[101], and (c) Z//[111]. Corresponding variations of maximum Schmid factors as the result of arbitrary rotation about the Z axis are provided in (d), (e), and (f), respectively.

Table 2
Summary of all simulations of cyclic loading of defect-free polycrystalline aggregates performed in this study (individual models are shown with a tick mark and the associated case numbers are written within the parentheses for each case).

	Z// [100]	Z//[101]		Z//[111]
Vertical	$\theta = 0.40$	$\theta = 0.40$		$\theta = 0.27$
$\lambda = 40$ μm	✓(1)	✓(3)		✓(5)
$\lambda = 60$ μm	✓(2)	✓(4)		✓(6)
Diagonal	$\theta = 0.44$	$\theta = 0.50$	$\theta = 0.35$	$\theta = 0.49$
$\lambda = 40$ μm	✓(7)	✓(9)	✓(11)	✓(13)
$\lambda = 60$ μm	✓(8)	✓(10)	✓(12)	✓(14)

For defect analysis, one specimen from each set of IN-718 batches fabricated for fatigue testing were cut into cuboids of ~3 × 4 × 5 mm and scanned using a Zeiss Xradia 620 Versa XCT machine. The imaging was performed at the source voltage and power of 160 kV and 25 W, respectively. An X-ray filter was used to minimize the count of low-energy photons. Following the reconstruction of the XCT obtained images, ImageJ software was used to analyze the defects via simple thresholding operations. The specimen was placed in the XCT machine such that the longest dimension of the cuboids was positioned vertically. The voxel size of the scans was ~3 μm in each direction. The defects of size (equivalent diameter) smaller than 5 μm were not included in the post processing to avoid false detection from artifacts. To confirm the defect analysis results obtained from XCT scanning, two-dimensional (2D) optical porosity analysis on the polished cross-sections of IN-718 specimens was also conducted using a Keyence optical microscope. For 2D porosity analysis, specimens were cut in a plane perpendicular to the build direction, mounted, and polished until they had a mirror finish. A minimum of five planes were analyzed for defect characterization of each sample. Defects population for a particular range of defect sizes were calculated based on the average values obtained from all readings.

Resulting data on defect distributions are presented in Fig. 8. As expected, the HIPed (i.e., coarse microstructure from HT2) IN-718 samples contains less defect compared the non-HIPed (i.e., fine microstructure from HT1) ones. Nevertheless, the overall trends of defect distribution in the size range of 5–20 μm for the fine microstructure were similar from both measurement techniques, even though the total defect count from optical microscopy was lower due to the limited cross-sections examined. The optical microscopy detected a few larger defects of size 20–25 μm in the fine microstructure, which were absent from the XCT scans. In addition, XCT scan did not detect any defects in the HT2 sample—only a small amount of relatively small defects were found by optical microscopy. These discrepancies between XCT and optical results could be due to the small volumes of the XCT samples (60 mm³) compared to the much larger volumes probed by cross-sectioning throughout the gage sections of the specimens shown in Fig. 10.

To assess the fatigue properties of IN-718 specimens, strain-controlled uniaxial fully-reversed fatigue tests ($R_\varepsilon = \varepsilon_{min} / \varepsilon_{max} = -1$) on HT1 and HT2 specimens were conducted. Tests utilized an MTS servo-hydraulic machine following the ASTM E606 standard [80]. An extensometer was attached to the specimen gages to monitor strain. Acrylic paint was applied to the attachment points to prevent slippage. Strain amplitudes ranged from 0.002 to 0.006 mm/mm. Test frequencies varied from 0.83 Hz for 0.002 mm/mm to 2.08 Hz for 0.006 mm/mm to ensure a constant nominal cyclic strain rate of 0.02 mm/mm/s. At least two specimens were tested for each strain amplitude. It is worth mentioning that during fatigue testing, specimens exceeding 10^7 reversals were stopped and considered as runout. Fractography was conducted on selected fracture surfaces of failed fatigue specimens using the SEM to investigate the failure mechanisms.
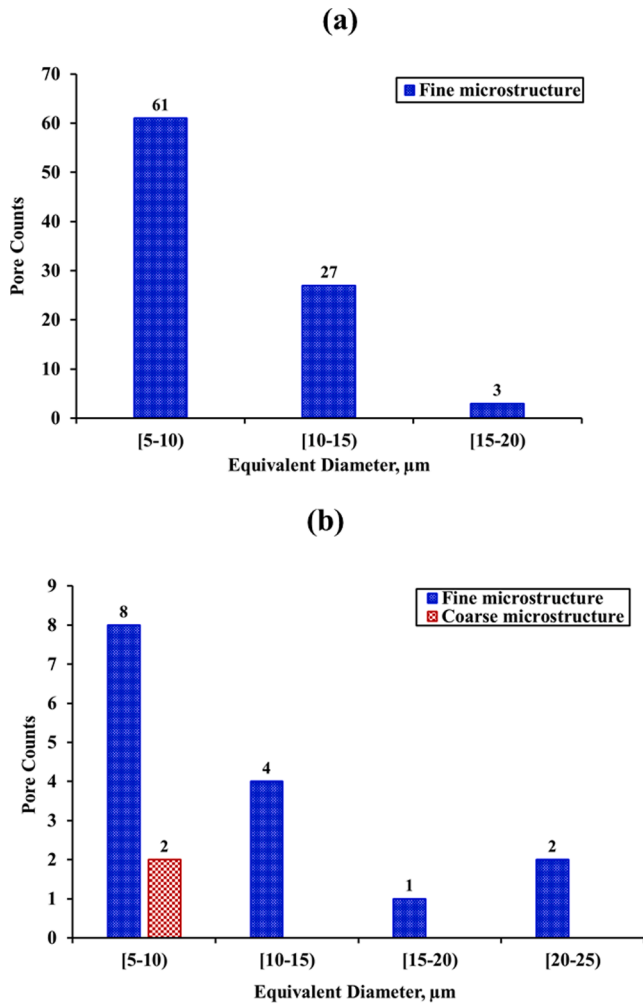
(a)

(b)

Fig. 8. Pore size distribution of LB-PBF IN-718 using (a) X-ray computed tomography and (b) optical microscopy.

4. Results and discussion

4.1. Strain localization behavior in the absence of volumetric defects

Utilizing the proposed location-dependent initial strength and hardening laws as stated in Eq. (7), strain localization within both the interior and boundaries of the central grain were captured by the CP simulations. The localization behavior appears to be affected by the crystallographic orientation of the central grain with respect to the loading directions. To visualize the cyclic strain distribution within the central grain, binning analyses were performed to visualize the cyclic shear strain amplitude on parallel crystallographic slip planes. For this purpose, the central grain was divided into slices parallel to slip planes, i.e., four different plane orientations for the FCC crystal structure of IN-718 (see Fig. 2 for schematic illustration). The average slip activity in each slice is calculated by taking the average of the von Mises strain among all voxels within the section at the load peak of each cycle. Thus, for each cycle, the average peak von Mises strain can be plotted

sequentially with respect to the slices, as shown in Fig. 11. Although the strain distributions on all four slip planes were examined, only the slice data on slip planes with the most prominent strain localization behaviors are visualized in this figure. It is apparent from Fig. 11 that the average von Mises strains were higher over a few sections compared to others – in some cases the higher strains occurred in Sections 1-9 (see Fig. 11 (a-f)), in other cases they occurred on Sections 0 & 10 (see Fig. 11(g-n)). Based on the location where the localization occurs, the cases can be categorized into two different groups; i.e., grain interior (GI) localization at Sections 1-9 and GB localizations at Sections 0 & 10. In all cases, as the number of cycles increased, the strain localization became more pronounced.

To further understand the factors influencing the strain localization behavior, the spatial distribution of the peak von Mises strain and maximum FSD were also visualized and analyzed. Two typical cases with GI localization (IDs #6 and #14) are exhibited in Fig. 12(a, b, d, and e), as examples. The distributions of von Mises strain amplitude shown for the cases in the figure corresponded to the certain cycles where the strain localization became apparent. Boundaries of the central grain are marked using black dashed lines. The FSD values shown in Fig. 12(a and d) were normalized against the maximum value in the respective case, and therefore, ranged between 0 and 1. The green arrows indicate the loading directions. In Fig. 12(b), clear strain localizations are notable by regions with relatively high strain values in the boxed area. In this case, the middle plane of the central grain was a (1 1 1) plane. The FSD values at this location (see Fig. 12(a)) were large which corresponded to low initial slip resistance and subsequent softening during cyclic loading. This likely has caused the localization.

However, the FSD was not the only factor governing the strain localization. For instance, case ID #14 had the central grain with the same orientation as the case ID #6, thus had the relatively high value of FSDs in the middle plane (see Fig. 12(d)). However, since it was loaded vertically, the location of GI strain localization apparently did not overlap with the crystallographic planes with the largest FSD (i.e., the (1 1 1) plane), rather it localized on the ($\bar{1}\bar{1}1$) plane. This observation appears to be consistent with the behavior of PSBs as their formation requires not only a relatively high FSD, but also sufficient resolved shear stress. The vertical loading direction of the example illustrated in Fig. 12 (d) resulted in essentially zero Schmid factor on the (1 1 1) plane which does not allow the formation of PSBs.

Given the observations made earlier, an intuitive parameter to evaluate the tendency for PSB formation is perhaps a compounded measure of both FSD and Schmid factor. Therefore, a localization parameter (δ) for a material point (or voxel) was defined in this work using the equation:

$$\delta = \max\left(\theta_\beta^t \times \eta_\beta^l\right) \text{ and } \beta = 1\ 4 \tag{11}$$

where θ is the averaged Schmid factor of all three slip systems that exist on the slip plane, β is the slip plane designator and ranges from 1 to 4 due to the four slip planes in an FCC lattice, η is the $\sqrt{area}$ of the grain's cross section through this point, and the exponents t and l assign the relative importance of resolved shear stress and FSD on the formation of PSB. Although at each material point there could be four distinct values of $\theta_\beta^t \times \eta_\beta^l$ depending (one value per slip plane, four planes total), only the maximum of which was assigned to δ. Based on the results of the CP simulations performed in this work, when t and l were respectively set to be 0.25 and 2, the resulting spatial distribution of maximum location

Table 3

Parameters in the isotropic plasticity material model intended for the pore region: Set 1 parameters are the actual ones used in the polycrystalline simulations; Set 2 parameters are used as a comparison to eliminate the Poisson's ratio and minimize the bulk modulus.

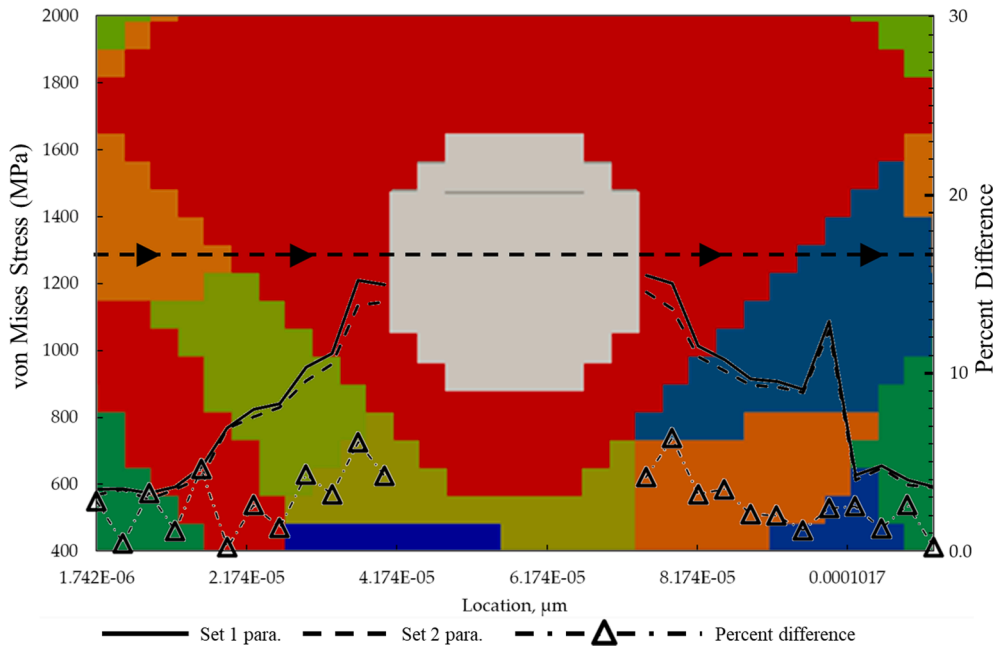| Set	C_{11}(GPa)	C_{44}(GPa)	$\dot{\gamma}_0$(s^{-1})	T	q(MPa)	a	ω^{ini} (MPa)	ω^{sat} (MPa)	h_0 (MPa)
1	259.6	109.6	0.01	20	4.0	2.5	0.02	0.5	0.075
2	25.0	1.0	0.01	20	4.0	2.5	0.02	0.5	0.075

Fig. 9. von Mises stress solutions of elastically deformed polycrystal including a pore. Left axis: von Mises stresses shown along the dashed arrow passing through the pore simulated with parameters sets listed in Table 3 (solid and dashed lines). Right axis: percent difference in the stress values (triangle marker with dashed dotted line).

Table 4
EOS M290 manufacturer recommended process parameters for IN-718.

Laser power	285 W
Scanning speed	960 mm/s
Layer thickness	40 μm
Hatching distance	110 μm

Fig. 10. The final dimension of fatigue specimens investigated in this study (All the dimensions are in mm).

parameter (δ) appeared to agree well with the spatial strain localization behavior observed in the simulations (i.e., good agreement between the type of graphs shown in Fig. 12(b & e) and the type shown in Fig. 12(e & f)). As a comparison with the FSD distributions, the respective distributions of the localization parameters are also provided in Fig. 12(c & f).

The spatial distribution of localization parameter (δ) appear to better agree with that of the cyclic von Mises strain. The same conclusion was found to be valid for other simulation cases with GI localizations.

4.2. Crack initiation behavior in the absence of defects

PSBs, which form after strain localization, are essentially pathways for plastic deformation where dislocation slip is significantly easier compared to other regions in a grain. As discussed in Section 2, this is due to the wall structures in the PSBs whose inter-wall spacing is much larger than the inter-bundle spacing in the matrix. As revealed by the CP simulations in this work and consistent with literature [33], the shear strain within the plane of strain localization was not constant and could vary due to a number of factors including the local stress concentrations at GBs. For instance, the contour plots of the von Mises strain for a few cases where strain localizes at the GI are shown in Fig. 13(a-d), where the localization slip planes are indicated using the red shades. The cycles at which the contour plots were generated are also given in the figure. Experimental observations revealed that shear strain amplitude within PSBs is constant within a material and is on the order of 0.01 ~0.02 mm/mm [37,85]. In this work, a simple criterion was defined for PSB formation: PSBs are said to have formed in a section if the peak von Mises strain exceeded 0.02 mm/mm in more than half of voxels in any cycle. Here, the von Mises strain, instead of the resolved shear strain on an interested section, was used to in the criterion because the plastic strain typically should not be confined within a single slip plane prior to the formation of PSBs. In fact, it has been shown that it was the "cross-cutting" action of dislocations, i.e., dislocations from the secondary slip planes gliding through veins, that collapsed the veins into walls [86]. Corresponding to the visualizations provided in Fig. 13(a-d), the
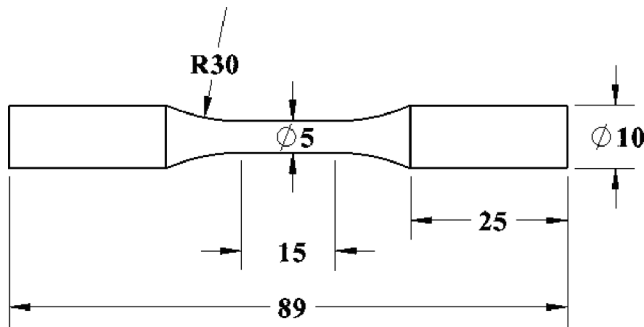
Table 5
Thermal and mechanical treatments applied for IN-718 specimens in this study, designated as Heat Treatments 1 and 2 (HT1 & HT2). FC: Furnace cooling, AC: Air cooling.

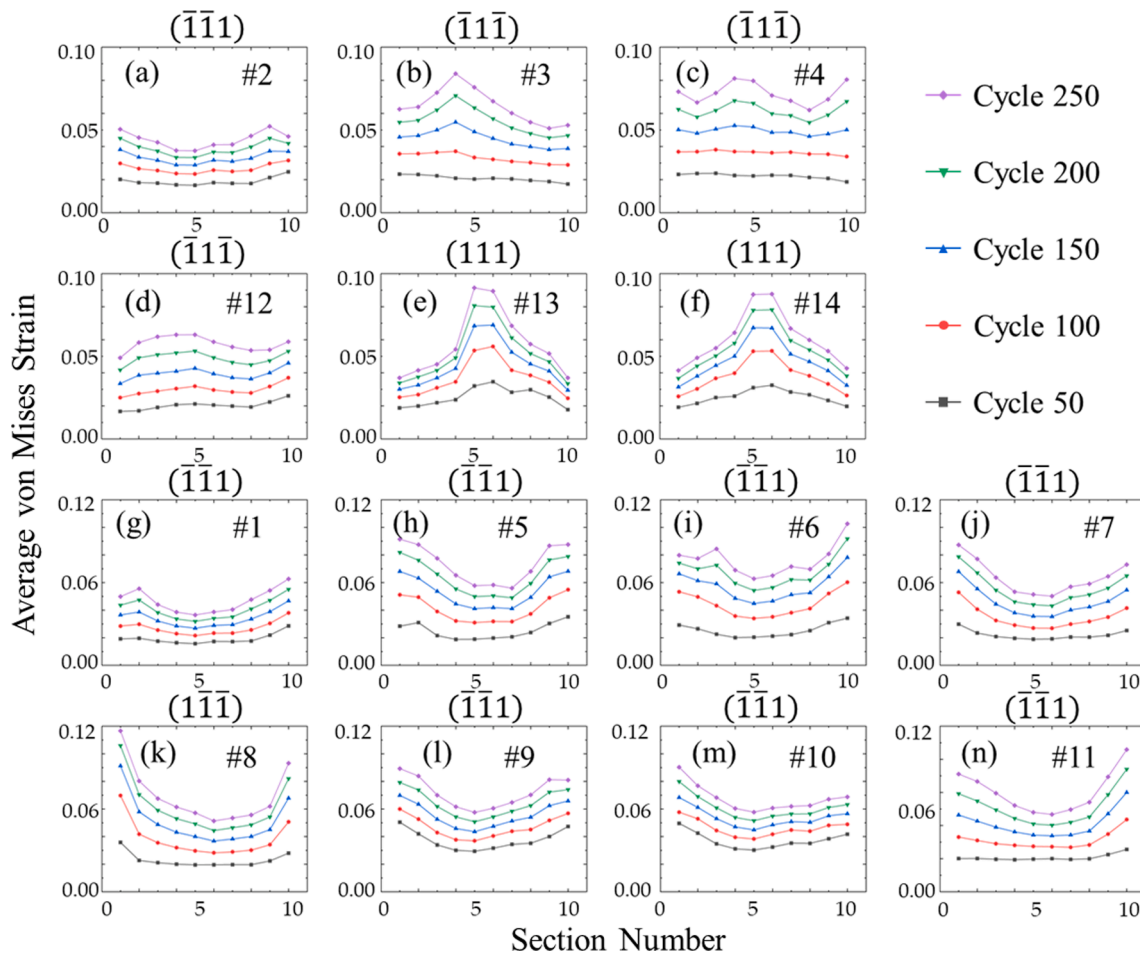| Designations	Stress relieving	Cooling	HIP	Solution treatment	Cooling	Ageing: Step 1	Ageing: Step 2	Cooling
HT1	1065 °C for 1.5 h	FC	–	1066 °C for 1 h	AC	760 °C for 10 h	650 °C for 10 h	AC
HT2	1065 °C for 1.5 h	FC	1163 °C at 102 MPa for 3 h	1066 °C for 1 h	AC	760 °C for 10 h	650 °C for 10 h	AC

Fig. 11. Average peak von Mises strain across the grain for the cases with grain interior (a-f) and grain boundary (g-n) localization. Strains are plotted sequentially with respect to the sections parallel to slip planes where localization behaviors were the most prominent. The slip planes as well as the IDs of the simulation cases are noted on each panel.
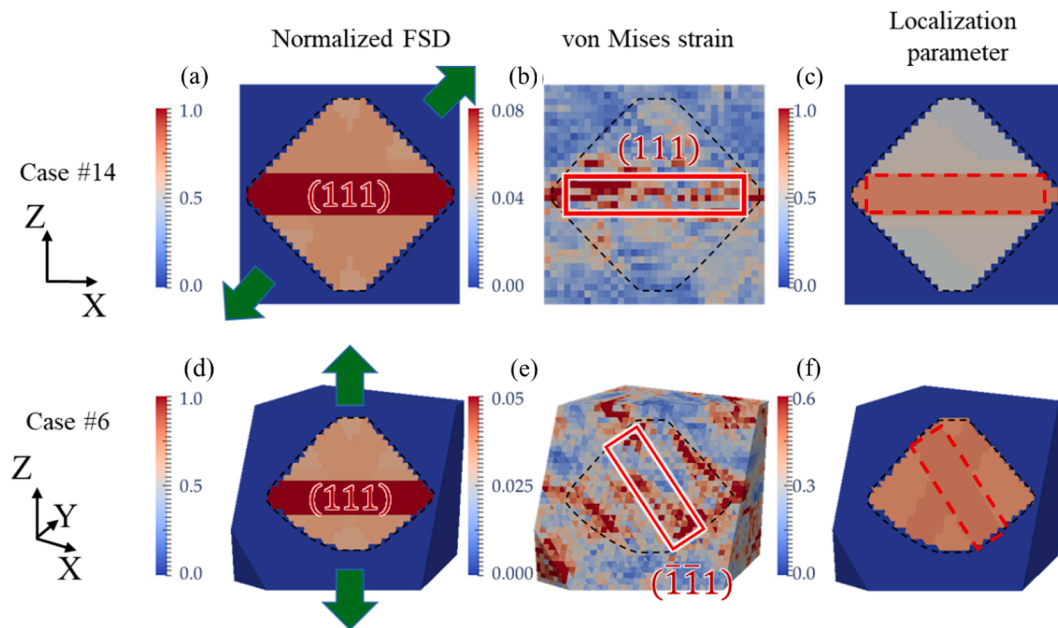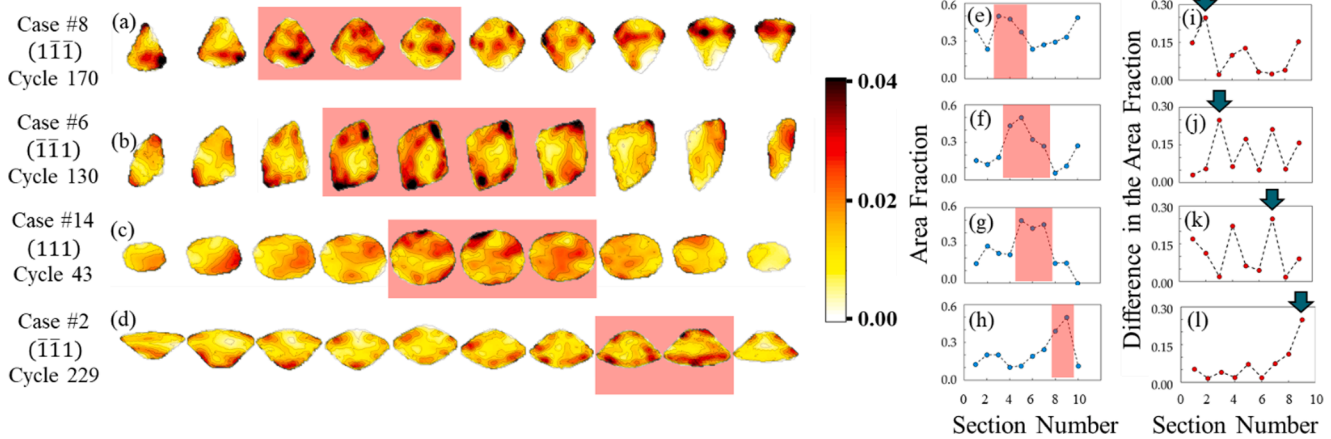

Fig. 12. Spatial distribution of (a, d) normalized FSD, (b, e) von Mises strain, and (c, f) localization parameter for 2 simulation cases with grain interior localization. First and second rows of panels correspond to case IDs #14 and #6, respectively.

Fig. 13. (a-d) Contour plots of the peak von Mises strain distribution for a few cases with grain interior localization at specific cycles. The case IDs, the cycle numbers, and the slip planes on which the contours were constructed are noted on the left. (e-h) The corresponding fraction of voxels within the sliced sections (or area fractions) whose von Mises strain were above 0.02 mm/mm. (k-n) The difference between the area fractions between the neighboring sections.

calculated fraction of voxels within the sliced sections (or area fractions) whose von Mises strain exceeded 0.02 is shown in Fig. 13(e-h). As shown in Fig. 13(a-h), the GI localization and the subsequent PSB formation occurred on the slip planes whose area (thus FSD) were largest among all parallel planar sections. Since these parallel sections had the same Schmid factor, these were also the locations where the localization parameters were the largest.

The PSB mediated initiation of fatigue cracks, as discussed in Section 2, typically occurs at PSB-matrix interface. This is because the operation of PSBs generates large amount of vacancies due to the forced-climb and annihilation of dislocations, which then diffuse and condense at the PSB-matrix interface (where abrupt changes in plastic strain occurs) rather than in the PSB interior [33,61,87]. Therefore, the contrast in the strain activities between the matrix and PSB—rather than the severity of plastic strains within a PSB—is a more relevant factor for crack initiation. On the other hand, at locations such as GBs, the elastic incompatibility between neighboring grains can induce significant near-GB plastic deformations under cyclic loading, incurring damage and leading to GB-mediated fatigue crack initiation without the presence of PSBs [88]. Therefore, strain localization observed adjacent to the GB shown in Fig. 11(g-n) can result in crack initiation. The PSB mediated and GB mediated modes compete to initiate fatigue cracks.

To this end, the differences in the area fractions shown in Fig. 13(b) between neighboring sections are computed and shown in Fig. 13(i-l). The PSB-matrix interfaces are distinguishable in the figure by spikes (indicated by arrows) where the differences between each two neighboring sections are large. The locations with the peak difference values (also indicated by arrows in Fig. 13(i-l)) are the primary candidates for crack initiation. Although Fig. 13 only visualizes four very typical cases of GI localization and crack initiation., the observations and discussions made are generally applicable to all simulation cases performed, including both GI and GB crack initiations. As a criterion, a crack can be said to have initiated on either side of the slip band if the difference in area fractions of two adjacent slices reaches a certain value. In this work, a value of 25% is used although a slightly deviation from it would not alter the overall observations in this study. For GB crack initiations, the same, slice-based criterion was applied. Using the criteria defined above for strain localization and crack initiation, the locations of strain localization as well as cycle number to crack initiation of all the simulation cases are summarized in Table 6.

Gathering data for all CP simulations, the maximum localization parameter in a given structure (δ_{max}) or its inverse versus the simulated lives to crack initiation (N_i) at GI and GBs are plotted in Fig. 14(a & b), respectively. For the cases where strain localization and PSB formation occur in the GI of the central grain, longer lives are observed for the

Table 6
Location and simulated cycles to crack initiation (N_i). V: vertically loaded specimen, D: Diagonally loaded specimen. The IDs of the simulation cases were also noted in the table.

λ (μm)	Z//[100]		Z//[101]			Z//[111]	
	V	D	V	D	D	V	D
40	#1: GB/ 195	#7: GI/ 175	#3: GB/ 84	#9: GB/ 171	#11: GB/116	#5: GB/ 183	#13: GI/37
60	#2: GI/ 229	#8: GI/ 170	#4: GB/ 82	#10: GB /130	#12: GB/135	#6: GI/ 130	#14: GI/43

simulated structures with smaller δ_{max}. In fact, the parameter and fatigue life to crack initiation appear to follow an inverse power law reasonably well (see Fig. 14(a)), indicating that higher resolved shear stress and larger FSD on certain slip planes favor fatigue crack initiation from the GI. For instance, when the [1 1 1] pole of the central grain aligns with the Z axis and loaded diagonally, the slip plane with the largest FSD and the one with highest Schmid factor coincides along the center line of the grain (see Fig. 12(a)). As a result, crack initiation criteria at the GI is met at ~40 simulated cycles (see in Fig. 14(a) as indicated by arrow as well as the data in Table 6).

While small maximum localization parameters extended the cycle life to crack initiation in the GI, excessively small values in this parameter can permit onset of the competing mechanism of the GB mediated crack initiation. In fact, very small resolved shear stresses and FSD values in a grain that suppress the GI crack initiation may favor the GB crack initiation, if the microstructure surrounding the grain of interest were to be kept constant. This trend is evident in Fig. 14(b), where an increasing trend between δ_{max} and crack initiation life via a power law exists among the GB crack initiation cases. For instance, relatively rapid crack initiation from GB has been observed at cycle ~80 when the low Schmid factors and small FSDs are combined, i.e., case IDs #3 and #4 (see in Fig. 14(b) as indicated by arrow as well as the data in Table 6). Overall, longer lives to fatigue crack initiation were observed for the GB crack initiation cases with larger δ_{max}.

In reality, the grains of both high and low δ values constitute a IN718 microstructure. Given that the literature-reported crack initiation modes had been either defect- or PSB- mediated for LB-PBF IN718, crack initiation in absence of defects should be transgranular within grains with high δ values—instead of at GBs near grains with low δ values. As an outlook, for alloys with relatively weak interfacial strengths, a competition between PSB-mediated and GB-mediated crack initiation
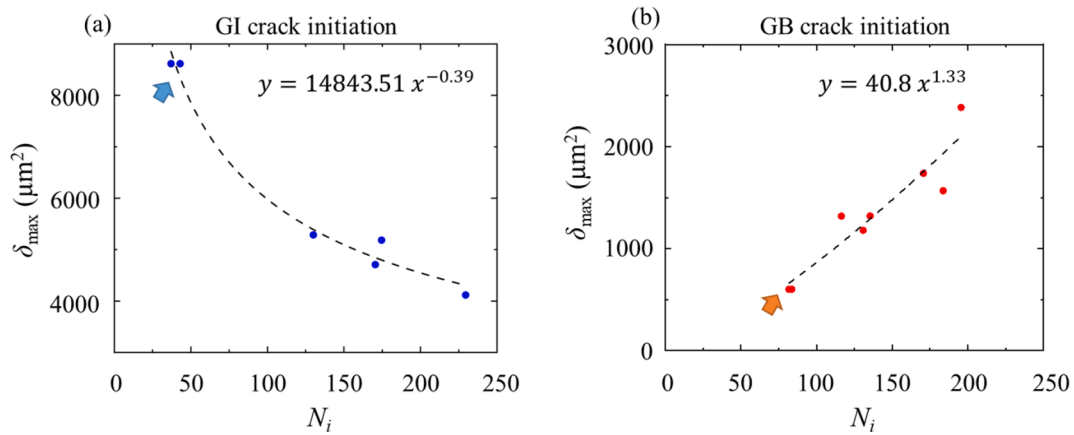
Fig. 14. Correlation between maximum localization parameter (δ_{max}) and simulated life to the crack initiation (N_i): (a) $\delta_{max} - N_i$ relation for GI initiation and (b) $1/\delta_{max} - N_i$ relation for GB initiation.

may exist [89]. Although the maximum localization parameter in an individual grain can be affected by its size and shape (which affect the FSD) as well as the loading direction (which affects the Schmid factor), the δ_{max} in a polycrystalline material without a strong texture and thus with a uniform distribution of Schmid factors—such as the HT IN-718 specimens examined in this work—is primarily influenced by the grain size. Therefore, one expects that the crack initiation mechanism of materials with finer microstructures to be more often GB dominated and that of the coarse-grained materials to be PSB dominated. This is consistent with the observations reported in the literature [21,39,40].

4.3. Effect of defect on strain localization and crack initiation

In the absence of defects, the previous sections demonstrated that the strain localization, PSB formation, and the subsequent crack initiation occur in the GI on the slip planes whose localization parameters are the largest, or on the GB if the maximum localization parameter is insufficient. These behaviors are expected to be similar to those of microstructures where the presence of defects is not critical to fatigue performance. Assuming for a moment that the shape of the defects is not a factor, the material volume around larger defects that experiences stress concentration is larger compared to that around the smaller defects, even though the stress concentration factors in both cases are the same. Larger defects therefore can impose stronger influence on the surrounding microstructure, may alter the behaviors of strain localization and the subsequent crack initiation, and be more critical to the fatigue behavior.

Defects observed in the XCT scans presented in Fig. 8 were all spherical in shape with varying sizes. This work is therefore primarily interested in the effect of defect size, rather than shape, on the strain localization and crack formation. To this end, a simulated defect-free microstructure (case ID #14) that has shown strain localization at middle plane ((1 1 1) plane) perpendicular to Z axis under diagonal loading (see for instance Fig. 12(a-c) & 16(c, g, & k)) is used to introduce defects. Three different defect diameters; i.e., 3.5, 10.5, and 17.5 μm are modeled in the same location with respect to the middle plane in the central grain (see illustration on the top of Fig. 15). For comparison, the distributions of peak von Mises strain on sequential (1 1 1) slices of the grain in the cycle of crack initiation are provided in Fig. 15. A total of 28 slices—each with the thickness of one voxel—are made for each simulation case. Slices with a higher area fractions of voxels (i.e., >20%) with peak von Mises strains higher than 0.02 are highlighted by red (Fig. 15 (a-c)) and yellow (Fig. 15(d)) shades to indicate the location of PSBs. The strain distribution for the defect-free case (case ID #14) is also provided in Fig. 15(a) for comparison. In Fig. 15(b-d), the slices through the volumetric defects are indicated by dashed boxes. Looking at the highlighted regions in Fig. 15(a-c), the slices with localized peak von Mises strain are similar with near-identical strain distributions when the defect size is ≤10.5 μm. However, when the defect size increases to 17.5 μm, the strain localization, while occurring over a narrower region (i.e., less slices), shifts towards the defect. The life to the crack initiation is similar for the first three cases; i.e., ~35 simulated cycles; however, it reduces to
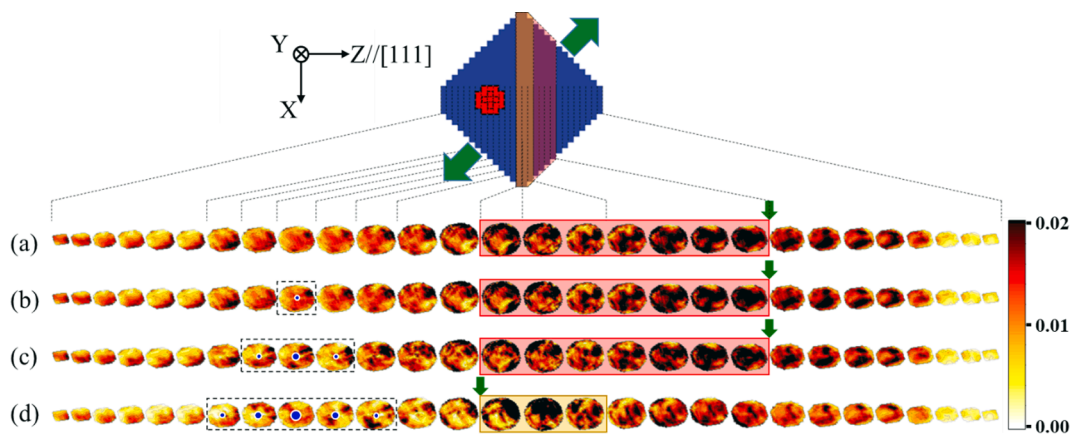

Fig. 15. Distribution of peak von Mises strains on (1 1 1) slices in the central grain: (a) defect-free case or simulation case ID #14, (b-d) with volumetric defects of varying diameter, i.e., 3.5 μm, 10.5 μm, and 17.5 μm, respectively. Locations of the slices with respect to the central grain are noted with dashed lines on the top of the figure. The green arrows denote the loading directions.

25 cycles when the pore size is the largest.

The visual observations provided in Fig. 15 are quantitatively presented in Fig. 16. In a fashion similar to Fig. 13(e-h), Fig. 16(a-d), the fractions of voxels (or area fraction) on each (1 1 1) slice of the central grain with peak von Mises strain greater than 0.02 at the formation of PSBs are presented. The cycles in which the maximum area fractions among all the slices achieved 0.5 were used to extract the data. As shown in Fig. 16, the distribution of peak von Mises strains does not appear to be significantly affected by the presence of the defects unless the defect is excessively large (i.e., 17.5 μm diameter). Schematic representations of the volumetric defects, with their varying size are also provided in the figure. Similar to Fig. 13(i-l), the differences in area fractions between neighboring slices at the onset of crack initiation are shown in Fig. 16(e-

h). Note that the data here was extracted from the cycles where the maximum difference for each case was 0.25. The locations of crack initiation site according to the criterion defined are indicated by green arrows. In the absence of defects, a crack initiates at Slice 20, according to the criterion defined in Section 4.2 (the contrast in area fraction >0.25). An increase in the defect size does not change the crack initiation site until the defect size is sufficiently large (~17.5 μm)— in which case the crack initiation shifts towards the pore.

4.4. Validation

The results of the CP simulations have so far demonstrated that two factors; i.e., FSD and Schmid factor, can influence the strain localization
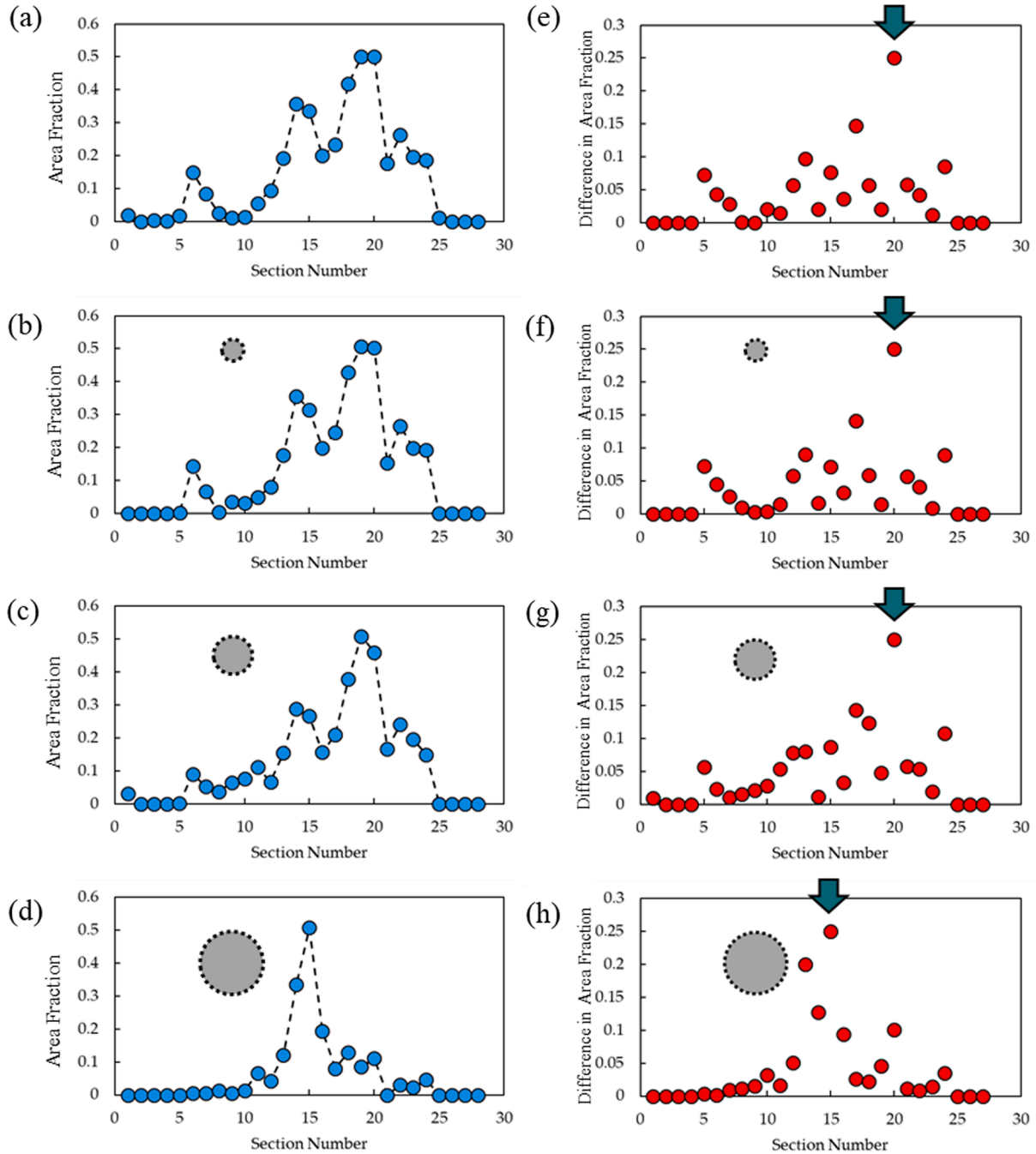

Fig. 16. (a-d) Profiles of average peak von Mises strain along [1 1 1] direction in the central grain of the simulation cases presented in Fig. 13. (e-h) The corresponding difference in area fraction between neighboring slices along [1 1 1] direction. Panels of (a,e), (b,f), (c,g), and (d,h) respectively present data from simulations with no defect, and with defects of diameters 3.5 μm, 10.5 μm, and 17.5 μm.

and the PSB driven crack initiation behaviors in IN-718. Within a grain, slip planes with larger combination of both factors, calculated as a localization parameter (δ defined in Eq. (11)), tend to localize cyclic strains and form PSBs. It followed that, a microstructure with larger maximum localization parameter (δ_{max}) is expected to have shorter fatigue crack initiation life. In addition, defects in IN-718 typically should not influence strain localization behavior unless their size is considerable compared to the grain size. To experimentally validate these findings, two HT schedules were applied on LB-PBF IN-718 specimens to induce fine (HT1) and coarse (HT2) microstructures, as listed in Table 5. In addition, HT2 included HIP so that the grain size could be increased to further reduced the ratio between the defects size and grain size compared to HT1.

Based on the IPF maps of HT1 and HT2 IN-718 specimens in radial and transverse planes presented in Fig. 5, the average grain size (equivalent circle diameter) for each case was also calculated according to the ASTM E2627 standard as 11.0 μm and 62.6 μm in radial planes and 14.5 μm and 69.8 μm in transverse planes, respectively [90]. Schmid factor maps in transverse planes for both HT1 and HT2 IN-718 specimens are also shown in Fig. 5(c & d). Fatigue data for the HT2 material set is listed in Table 7. The strain-life data reported by Lee et al. [81], where fatigue tests were performed on the specimens whose dimensions were identical with what was given in Fig. 10 and whose microstructure was identical to the HT1 condition shown in Fig. 5, is included in this study. However, the strain-life fatigue data for HT2 is generated in this work. Strain-life fatigue behaviors of IN-718 specimens undergone both HT1 [81] and HT2 are plotted in Fig. 17. Runout tests are indicated by arrows on the figure. As is evident in Fig. 17, longer lives to failure at all strain amplitudes are obtained for HT1 specimens (smaller grain size), even though HT2 specimens are HIPed.

While there are some differences in fatigue lives between the two specimen sets at the higher strain amplitudes, these differences become more significant as the strain amplitude decreases. At the higher strain amplitude of 0.0050 mm/mm, where crack growth stage dominates a higher portion of the overall fatigue process, the difference in fatigue lives between HT1 and HT2 sets was only a factor of 2–3. On the other hand, at the lower strain amplitude of 0.0030 mm/mm, where crack initiation is more important, at least one order of magnitude longer average fatigue life was measured for fine grained specimen set (HT1). At the even lower strain amplitude of 0.0027 mm/mm, while all HT1 specimens exceeded 10^7 reversals, all the HT2 specimens failed below 10^6 reversals.

Crystallographic facets were also observed in the crack initiation sites on all the fracture surfaces in both specimen sets (see Fig. 18)—volumetric defects were not seen in the crack initiating regions. Overall, facets visible from the fracture surfaces of the HT2 specimens (Fig. 18 (b)) were typically larger compared to those of the HT1 specimens (Fig. 18(a)). The size of the facets was measured as their $\sqrt{area}$ projected on the loading plane and the average values were reported for specimens failed at different strain amplitudes in Table 8. The values of each strain
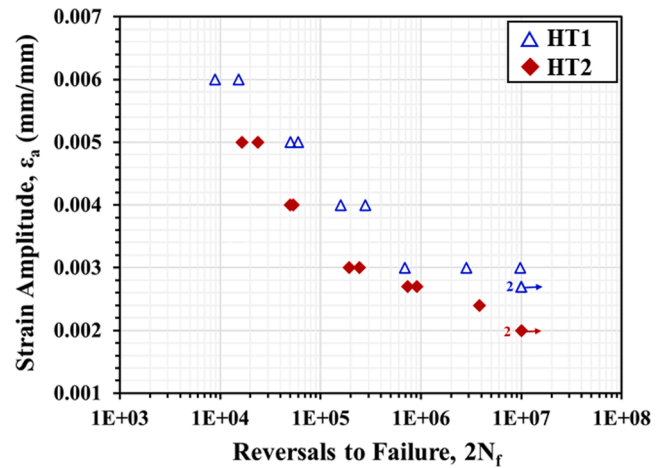

Fig. 17. Strain-life fatigue behaviors of HT1 and HT2 IN-718 specimens. HT1 specimens were tested in this work, while the data for HT1 specimens was obtained from Lee et al. [81].

amplitude were calculated based on a minimum of 3 measurements. Independent of the loading amplitudes, the average facet sizes appear to be similar within a specimen set. The average $\sqrt{area}$ of the facets for HT1 set (i.e., fine grains) is ~80 μm and for HT2 (i.e., coarse grains) is ~220 μm—a difference by a factor of 2.75. These facet sizes are comparable to the sizes of the large grains in the two specimen sets (compare Figs. 5 and 6, where HT1 and HT2 consists of large grains of ~100 μm and ~250 μm in the radial plane, respectively).

Considering that the maximum Schmid factors in both microstructures are comparable as shown in Fig. 5(c & f), the localization parameter for the two specimen sets can be estimated solely using the average size of the large grains and assuming an identical mean Schmid factor. The localization parameter (δ_{max}) for HT1 is smaller than that of the HT2 by a factor of 6.74. According to Fig. 14(a), the localization parameter and the simulated cycle life to GI crack initiation follow an inversed power law, i.e., $\delta_{max} = 14843.51 N_f^{-0.39}$. Dictated by this power law relation, a smaller localization parameter of the finer microstructure by a factor of 6.74 would lead to 133 times longer life to crack initiation for the HT1 specimens as compared to the HT2 ones. This appears to agree well with the fatigue lives measured for both specimen sets under strain amplitudes of 0.0030 mm/mm or lower. Under these amplitudes, fatigue life was in the HCF regime and was dominated by crack initiation—in fact, the lower the strain amplitude the higher life fraction crack initiation occupied. At 0.0030 mm/mm, the fatigue life of HT1 and HT2 specimens differed by an order of magnitude; at 0.0027 mm/mm, the difference was more than one order of magnitude as all HT1 specimens ran out. Noting that the spread of data at 0.0030 mm/mm level for HT1 specimens was more than a decade and the spread tended to increase

Table 7
Strain-controlled fatigue test data of HT2 LB-PBF IN-718 specimen.

| Specimen	ID	Total strain amplitude, ε_a (mm/mm)	Elastic strain amplitude, ε_e (mm/mm)	Plastic strain amplitude, ε_p (mm/mm)	Stress amplitude, σ_a (MPa)	Mean stress, σ_m (MPa)	Reversals to failure, $2N_f$
HT2	B08	0.0020	0.0020	0.0000	362	−1	>1.00E+07
IN-718	B09	0.0020	0.0020	0.0000	368	−4	>1.00E+07
	B02	0.0024	0.0024	0.0000	433	−17	3.84E+06
	B01	0.0027	0.0027	0.0000	492	−18	9.10E+05
	B10	0.0027	0.0027	0.0000	489	−26	7.40E+05
	B03	0.0030	0.0030	0.0000	527	−3	2.44E+05
	B07	0.0030	0.0030	0.0000	530	0	1.92E+05
	B12	0.0040	0.0040	0.0000	721	−23	5.36E+04
	B06	0.0040	0.0040	0.0000	709	−28	4.98E+04
	B05	0.0050	0.0049	0.0001	861	−6	2.37E+04
	B04	0.0050	0.0049	0.0001	870	−10	1.64E+04
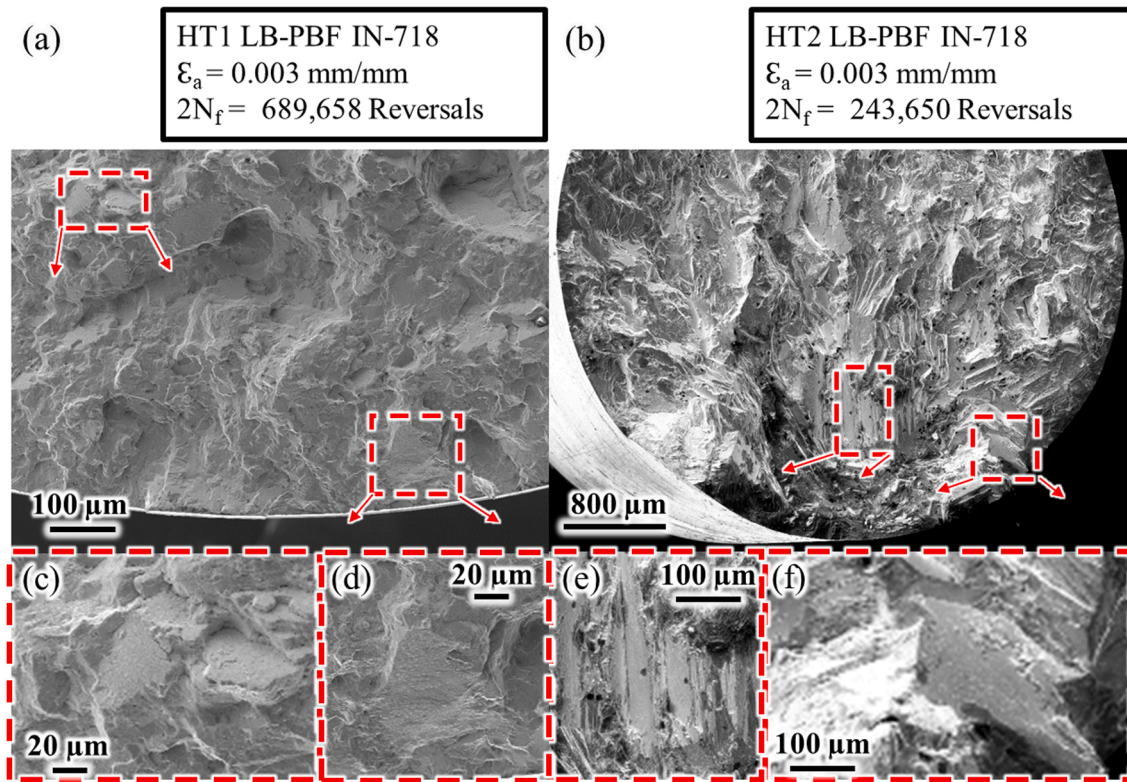
Fig. 18. The fracture surfaces of (a) an HT1 specimen, and (b) an HT2 specimen. Selected regions of the fracture surfaces are magnified to provide details of the crack initiation sites in (c-f).

Table 8
The average facet root area measured from the fracture surfaces of IN-718 fatigue specimens.

Strain amplitude (mm/mm)	HT1 (µm)	HT2 (µm)
0.0027	Run-out	244
0.0030	113	212
0.0040	66	266
0.0050	59	178

with decreasing strain level, the difference between the average lives of HT1 and HT2 specimens was expected to be at least two decades at 0.0027 mm/mm had the tests ran to failure.

Longitudinal cross sections of the fractured specimens were also polished and examined to reveal the formation mechanism of the facets. Fig. 19 provides ECCI micrographs on regions near the crack initiation site on the longitudinal cross section of a fractured HT2 specimen failed under strain amplitude of 0.0050 mm/mm. It is evident that strain localization occurred and PSBs formed at several locations. Under higher magnification (Fig. 19(c-d)), small voids whose sizes are approximated hundreds of nm, uniformly distributed throughout the volume, are also visible. These voids are also present in the non-tested microstructures, and are believed to be small gas entrapped pores that typically form during the fabrication process. What is also interesting to note is the linear arrays of voids that formed along the PSBs. These arrays contain high density of voids and are preferred path for fatigue crack initiation. Some cracks initiated along the PSBs are also visible in Fig. 19(a-b)—some of these cracks are in fact the extension of facets on the fracture surface.

The ECCI micrograph of the longitudinal cross section of a failed specimen in Fig. 20 shows a large grain adjacent to the fracture surface at the crack initiation site. It is noticeable that the formation of PSBs is not uniform throughout the grain. Instead, they tend to form along slip

planes whose FSDs are greater, which is qualitatively in agreement with the predictions made based on the CP simulations. Multiple parallel PSBs close to the fracture surface are visible in the grain, especially in the magnified view in Fig. 20(b) as indicated by the red arrow. These PSBs are parallel to a facet formed on the fracture surface, which suggests that the crack may have propagated along one of these PSBs while branching to other planes. In addition, the slip activity within the dashed region between two small grains in Fig. 20(b) appears to have been impeded by the relatively small FSD, resulting in the absence of any apparent slip markings in this region.

The slip planes on which the PSBs (as indicated by the red arrow in Fig. 20(b)) were formed are denoted as SP1. As shown in Fig. 20(b), the trace of SP1 coincides with the coherent twin boundary of an annealing twinning (CTB1). The presence of another coherent twin boundary (CTB2) in Fig. 20(a) indicates the trace of another slip plane (SP2). From the orientation contrast offered by the ECCI technique, it appears that the maximum FSD values along SP1 and SP2 could both be relatively large. The fact that the PSBs only exist on SP1 may be explained by the localization parameters proposed in this work. With data from EBSD scans performed at this location, Fig. 20(c-d) present the distribution of FSD (or η) parameter within this grain along SP1 and SP2, respectively. In lieu of information on the grain geometry in the depth direction of the micrographs, the free distances (i.e., distances between the closest obstacles) along the traces of SP1 and SP2 were calculated. The calculated maximum FSD along these two slip planes are both very large at ~450 µm. The absence of PSBs on SP2 may be related to the difference in Schmid factors. Indeed, EBSD scans reveal that the average Schmid factors on SP1 is 0.32, while that for SP2 is only 0.10. As a result, the calculated maximum localization parameter (δ_{max}) along SP1 is higher as shown in Fig. 20 (e-f). It is also very interesting to note that the location of where the maximum localization parameter has occurred well-coincides with the location where the PSBs are formed in the grain (compare Fig. 20(e) with Fig. 20(a-b)).
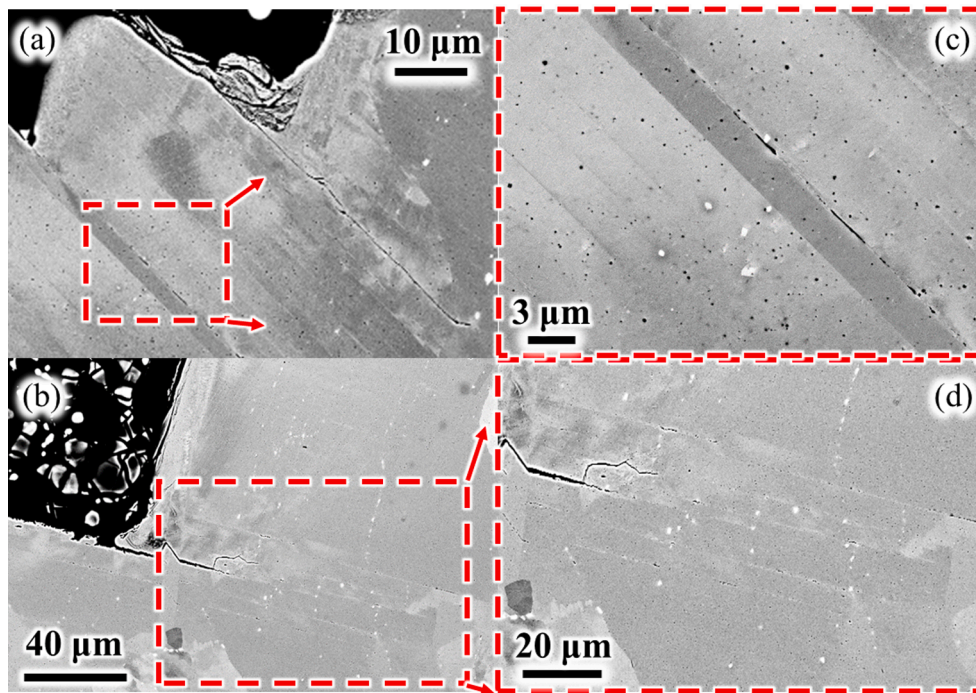
Fig. 19. ECCI micrographs on the vertical cross-section of a HT2 specimen failed under strain amplitude of 0.005 mm/mm with magnified views provided in (c & d).
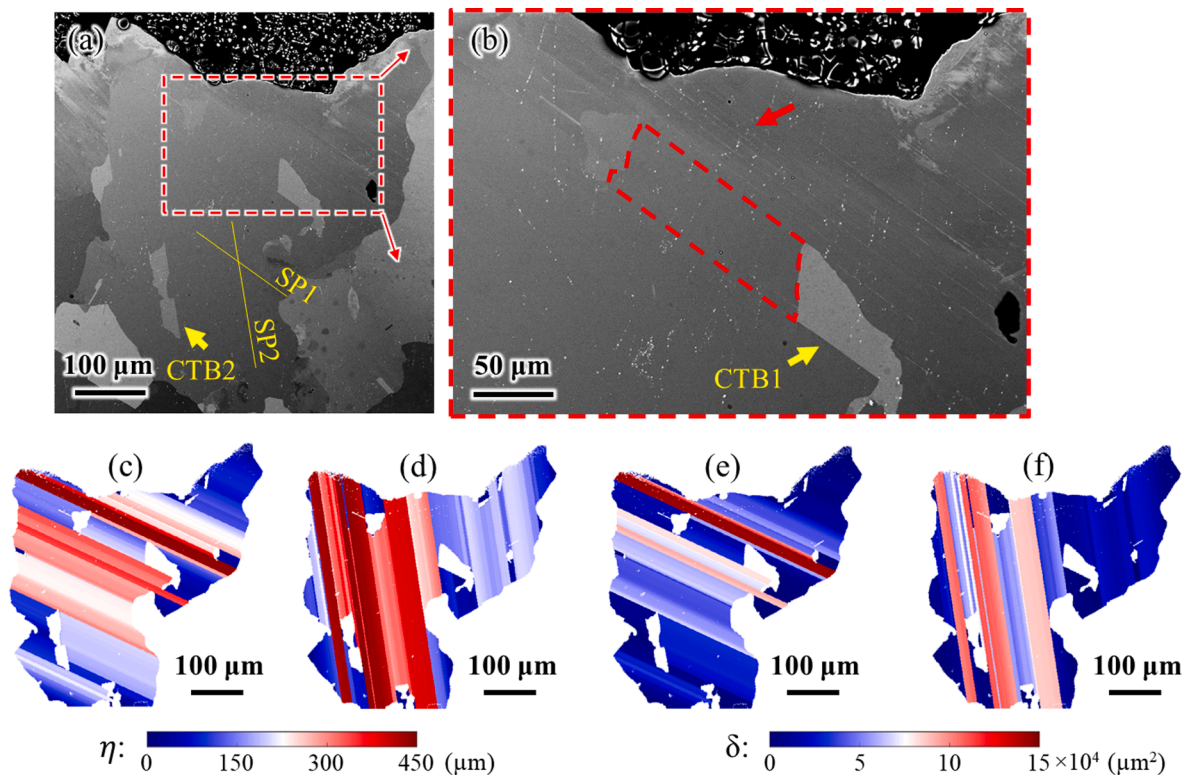

Fig. 20. (a) Slip markings parallel to the planar features formed on the fracture surface, and (b) formation of faceted regions on the fracture surface as a result of crack growth on these facets.

5. Conclusion

In this work, CP simulations were performed to shed light on the fatigue crack initiation mechanisms in laser beam powder bed fused (LB-PBF) IN-718. With a new material strength model and a new crack initiation criterion, the strain localization and fatigue crack initiation behaviors were investigated. Specifically, the effects of FSD, Schmid factor, and volumetric defects were studied in detail. The major findings obtained from the CP simulations were validated against experimental observations via extensive microstructural characterization, mechanical testing, and failure analysis. The following conclusions can be drawn from this study:

1. CP simulations revealed that the location of strain localization, i.e., grain interiors versus grain boundaries, was strongly affected by both the free slip distance and the Schmid factors on slip planes. A localization parameter was defined for each material point based on the multiplication of the two factors raised to different powers. Regions with high values of localization parameters in a grain were found to localize cyclic strains.

2. The maximum value of the localization parameter in a microstructure correlated with its life to fatigue crack initiation. Larger maximum values of this parameter would result in earlier crack initiation from the grain interior. On the contrary, lower maximum values of this parameter tended to delay the crack initiation in the grain, and thus, promote crack initiation at grain boundaries.

3. The existence of defects did not affect the strain localization behavior and life to crack initiation unless they occupied a significant portion of the grain. A larger defect could shorten the fatigue life and shift the location of the PSBs/crack initiation sites towards the defect.

4. Results from strain-controlled fatigue tests performed on heat treated LB-PBF IN-718 with both coarse and fine microstructure supported the findings from simulations. Fractography revealed that initiation of all fatigue cracks was due to the damage in the form of void arrays accumulated from the operation of PSBs in larger grains instead of from smaller defects.

5. Coarser microstructure with larger FSD values showed lower resistance to crack initiation. This lead to significantly lower fatigue lives (more than one order of magnitude) at lower strain amplitudes (i.e., high cycle fatigue regime), where the crack initiation occupies a larger fraction of life. PSBs as seen in the experiment tended to form at slip planes in a grain whose localization parameter was the highest.

Declaration of Competing Interest

The authors declare that they have no known competing financial interests or personal relationships that could have appeared to influence the work reported in this paper.

Disclaimer

This report was prepared as an account of work sponsored by an agency of the United States Government. Neither the United States Government nor any agency thereof, nor any of their employees, makes any warranty, express or implied, or assumes any legal liability or responsibility for the accuracy, completeness, or usefulness of any information, apparatus, product, or process disclosed, or represents that its use would not infringe privately owned rights. Reference herein to any specific commercial product, process, or service by trade name, trademark, manufacturer, or otherwise does not necessarily constitute or imply its endorsement, recommendation, or favoring by the United States Government or any agency thereof. The views and opinions of authors expressed herein do not necessarily state or reflect those of the United States Government or any agency FA R&D Special TC NOVEMBER 2017- FF Page 4 of 12 thereof.

References

[1] Shamsaei N, Yadollahi A, Bian L, Thompson SM. An overview of Direct Laser Deposition for additive manufacturing; Part II: mechanical behavior, process parameter optimization and control. Addit Manuf 2015;8:12–35. https://doi.org/10.1016/j.addma.2015.07.002.

[2] Thompson SM, Bian L, Shamsaei N, Yadollahi A. An overview of Direct Laser Deposition for additive manufacturing; Part I: transport phenomena, modeling and diagnostics. Addit Manuf 2015;8:36–62. https://doi.org/10.1016/j.addma.2015.07.001.

[3] Yadollahi A, Shamsaei N. Additive manufacturing of fatigue resistant materials: Challenges and opportunities. Int J Fatigue 2017;98:14–31. https://doi.org/10.1016/j.ijfatigue.2017.01.001.

[4] Molaei R, Fatemi A, Sanaei N, Pegues J, Shamsaei N, Shao S, et al. Fatigue of additive manufactured Ti-6Al-4V, Part II: The relationship between microstructure, material cyclic properties, and component performance. Int J Fatigue 2020;132: 105363. https://doi.org/10.1016/j.ijfatigue.2019.105363.

[5] Pegues JW, Shao S, Shamsaei N, Sanaei N, Fatemi A, Warner DH, et al. Fatigue of additive manufactured Ti-6Al-4V, Part I: The effects of powder feedstock, manufacturing, and post-process conditions on the resulting microstructure and defects. Int J Fatigue 2020;132:105358. https://doi.org/10.1016/j.ijfatigue.2019.105358.

[6] Nezhadfar PD, Anderson-Wedge K, Daniewicz SR, Phan N, Shao S, Shamsaei N. Improved high cycle fatigue performance of additively manufactured 17–4 PH stainless steel via in-process refining micro-/defect-structure. Addit Manuf 2020; 36:101604. https://doi.org/10.1016/j.addma.2020.101604.

[7] Shrestha R, Simsiriwong J, Shamsaei N. Fatigue behavior of additive manufactured 316L stainless steel under axial versus rotating-bending loading: Synergistic effects of stress gradient, surface roughness, and volumetric defects. Int J Fatigue 2021; 144:106063. https://doi.org/10.1016/j.ijfatigue.2020.106063.

[8] Beretta S. More than 25 years of extreme value statistics for defects: Fundamentals, historical developments, recent applications. Int J Fatigue 2021;151:106407. https://doi.org/10.1016/j.ijfatigue.2021.106407.

[9] Hamidi Nasab M, Romano S, Gastaldi D, Beretta S, Vedani M. Combined effect of surface anomalies and volumetric defects on fatigue assessment of AlSi7Mg fabricated via laser powder bed fusion. Additive Manuf 2019;1. https://doi.org/10.1016/j.addma.2019.100918.

[10] Lingenfelter A. Welding of Inconel Alloy 718: A Historical Overview, in: Superalloys 718 Metallurgy and Applications (1989), TMS; 1989: pp. 673–683. https://doi.org/10.7449/1989/Superalloys_1989_673_683.

[11] Siddique S, Awd M, Tenkamp J, Walther F. High and very high cycle fatigue failure mechanisms in selective laser melted aluminum alloys. J Mater Res 2017;32: 4296–304. https://doi.org/10.1557/jmr.2017.314.

[12] Mostafaei A, Zhao C, He Y, Reza Ghiaasiaan S, Shi Bo, Shao S, et al. Defects and anomalies in powder bed fusion metal additive manufacturing. Curr Opin Solid State Mater Sci 2022;26(2):100974.

[13] Muhammad M, Frye P, Simsiriwong J, Shao S, Shamsaei N. An investigation into the effects of cyclic strain rate on the high cycle and very high cycle fatigue behaviors of wrought and additively manufactured Inconel 718. Int J Fatigue 2021; 144:106038. https://doi.org/10.1016/j.ijfatigue.2020.106038.

[14] Nezhadfar PD, Johnson AS, Shamsaei N. Fatigue behavior and microstructural evolution of additively manufactured Inconel 718 under cyclic loading at elevated temperature. Int J Fatigue 2020;136:105598. https://doi.org/10.1016/j.ijfatigue.2020.105598.

[15] Kotzem D, Dumke P, Sepehri P, Tenkamp J, Walther F. Effect of miniaturization and surface roughness on the mechanical properties of the electron beam melted superalloy Inconel®718. Progr Additive Manuf 2020;5:267–76. https://doi.org/10.1007/s40964-019-00101-w.

[16] Wan H-Y, Zhou Z-J, Li C-P, Chen G-F, Zhang G-P. Enhancing Fatigue Strength of Selective Laser Melting-Fabricated Inconel 718 by Tailoring Heat Treatment Route. Adv Eng Mater 2018;20:1800307. https://doi.org/10.1002/adem.201800307.

[17] Yang K, Huang Q, Wang Q, Chen Q. Competing crack initiation behaviors of a laser additively manufactured nickel-based superalloy in high and very high cycle fatigue regimes. Int J Fatigue 2020;136:105580. https://doi.org/10.1016/j.ijfatigue.2020.105580.

[18] Tiryakioğlu M, Campbell J, Nyahumwa C. Fracture Surface Facets and Fatigue Life Potential of Castings. Metall Mater Trans B 2011;42:1098–103. https://doi.org/10.1007/s11663-011-9577-3.

[19] Differt K, Esmann U, Mughrabi H. A model of extrusions and intrusions in fatigued metals II. Surface roughening by random irreversible slip. Philos Mag A 1986;54: 237–58. https://doi.org/10.1080/01418618608242897.

[20] Mughrabi H. Microstructural mechanisms of cyclic deformation, fatigue crack initiation and early crack growth. Philos Trans Royal Soc A: Math, Phys Eng Sci 2015;373:20140132. https://doi.org/10.1098/rsta.2014.0132.

[21] Essmann U, Gösele U, Mughrabi H. A model of extrusions and intrusions in fatigued metals I. Point-defect production and the growth of extrusions. Philos Mag A 1981; 44:405–26. https://doi.org/10.1080/01418618108239541.

[22] Mughrabi H. Damage Mechanisms and Fatigue Lives: From the Low to the Very High Cycle Regime. Procedia Eng 2013;55:636–44. https://doi.org/10.1016/j.proeng.2013.03.307.

[23] Kang G, Dong Y, Wang H, Liu Y, Cheng X. Dislocation evolution in 316L stainless steel subjected to uniaxial ratchetting deformation. Mater Sci Eng, A 2010;527: 5952–61. https://doi.org/10.1016/j.msea.2010.06.020.

[24] Li XW, Hu YM, Wang ZG. Investigation of dislocation structure in a cyclically deformed copper single crystal using electron channeling contrast technique in SEM. Mater Sci Eng, A 1998;248:299–303. https://doi.org/10.1016/S0921-5093(98)00501-2.

[25] Li P, Zhang ZF, Li SX, Wang ZG. Cyclic deformation and fatigue damage behaviors of oriented Ag single crystal. Phil Mag 2009;89:2903–20. https://doi.org/10.1080/14786430903130847.

[26] Li P, Li SX, Wang ZG, Zhang ZF. Dislocation arrangements in cyclically deformed Au single crystal. Mater Sci Eng, A 2010;527:6244–7. https://doi.org/10.1016/j.msea.2010.06.040.

[27] Shao S, Khonsari MM, Guo S, Meng WJ, Li N. Overview: Additive Manufacturing Enabled Accelerated Design of Ni-based Alloys for Improved Fatigue Life. Addit Manuf 2019;29:100779. https://doi.org/10.1016/j.addma.2019.100779.

[28] Dodaran M, Khonsari MM, Shao S. Critical operating stress of persistent slip bands in Cu. Comput Mater Sci 2019;165:114–20. https://doi.org/10.1016/j.commatsci.2019.04.036.

[29] Brown LM. Dislocation bowing and passing in persistent slip bands. Phil Mag 2006; 86:4055–68. https://doi.org/10.1080/14786430500501689.

[30] Neumann P. Dislocation dynamics in fatigue. Phys Scr 1987;T19B:537–43.

[31] Kuhlmann-Wilsdorf D, Laird C. Dislocation behavior in fatigue. Mater Sci Eng 1977;27:137–56. https://doi.org/10.1016/0025-5416(77)90166-5.

[32] Kuhlmann-Wilsdorf D. Theory of plastic deformation: - properties of low energy dislocation structures. Mater Sci Eng, A 1989;113:1–41. https://doi.org/10.1016/0921-5093(89)90290-6.

[33] Bao-Tong M, Laird C. Overview of fatigue behavior in copper single crystals—I. Surface morphology and stage I crack initiation sites for tests at constant strain amplitude. Acta Metallurgica 1989;37:325–36. https://doi.org/10.1016/0001-6160(89)90217-4.

[34] Hunsche A, Neumann P. Quantitative measurement of persistent slip band profiles and crack initiation. Acta Metall 1986;34:207–17. https://doi.org/10.1016/0001-6160(86)90192-6.

[35] Sangid MD, Maier HJ, Sehitoglu H. A physically based fatigue model for prediction of crack initiation from persistent slip bands in polycrystals. Acta Mater 2011;59: 328–41. https://doi.org/10.1016/j.actamat.2010.09.036.

[36] Mughrabi H. Cyclic Slip Irreversibilities and the Evolution of Fatigue Damage. Metall Mater Trans A 2009;40:1257–79. https://doi.org/10.1007/s11661-009-9839-8.

[37] Dodaran MS, Wang J, Shamsaei N, Shao S. Investigating the Interaction between Persistent Slip Bands and Surface Hard Coatings via Crystal Plasticity Simulations. Crystals (Basel) 2020;10:1012. https://doi.org/10.3390/cryst10111012.

[38] Thompson AW, Backofen WA. The effect of grain size on fatigue. Acta Metall 1971; 19:597–606. https://doi.org/10.1016/0001-6160(71)90012-5.

[39] Stinville J-C, Martin E, Karadge M, Ismonov S, Soare M, Hanlon T, et al. Competing Modes for Crack Initiation from Non-metallic Inclusions and Intrinsic Microstructural Features During Fatigue in a Polycrystalline Nickel-Based Superalloy. Metall Mater Trans A 2018;49:3865–73. https://doi.org/10.1007/s11661-018-4780-3.

[40] Keller R, Zielinski W, Gerberich WW. On the onset of low-energy dislocation substructures in fatigue: Grain size effects. Mater Sci Eng, A 1989;113:267–80. https://doi.org/10.1016/0921-5093(89)90315-8.

[41] Zhang GP, Schwaiger R, Volkert CA, Kraft O. Effect of film thickness and grain size on fatigue-induced dislocation structures in Cu thin films. Philos Mag Lett 2003;83: 477–83. https://doi.org/10.1080/0950083031000151383.

[42] Polák J, Man J. Fatigue crack initiation – The role of point defects. Int J Fatigue 2014;65:18–27. https://doi.org/10.1016/j.ijfatigue.2013.10.016.

[43] Polák J, Lepistö T, Kettunen P. Surface topography and crack initiation in emerging persistent slip bands in copper single crystals. Mater Sci Eng 1985;74:85–91. https://doi.org/10.1016/0025-5416(85)90112-0.

[44] Man J, Vystavěl T, Weidner A, Kuběna I, Petrenec M, Kruml T, et al. Study of cyclic strain localization and fatigue crack initiation using FIB technique. Int J Fatigue 2012;39:44–53. https://doi.org/10.1016/j.ijfatigue.2011.05.002.

[45] Hu YM, Wang ZG. Grain boundary effects on the fatigue deformation and cracking behavior of copper bicrystals. Int J Fatigue 1998;20:463–9. https://doi.org/10.1016/S0142-1123(98)00014-0.

[46] Man J, Klapetek P, Man O, Weidner† A, Obrtlík K, Polák J. Extrusions and intrusions in fatigued metals. Part 2. AFM and EBSD study of the early growth of extrusions and intrusions in 316L steel fatigued at room temperature. Phil Mag 2009;89(16):1337–72.

[47] Man J, Obrtlík K, Polák J. Extrusions and intrusions in fatigued metals. Part 1. State of the art and history. Phil Mag 2009;89:1295–336. https://doi.org/10.1080/14786430902021616.

[48] Babinský T, Kuběna I, Šulák I, Kruml T, Tobiáš J, Polák J. Surface relief evolution and fatigue crack initiation in René 41 superalloy cycled at room temperature. Mater Sci Eng, A 2021;819:141520. https://doi.org/10.1016/j.msea.2021.141520.

[49] Weidner A, Beyer R, Blochwitz C, Holste C, Schwab A, Tirschler W. Slip activity of persistent slip bands in polycrystalline nickel. Mater Sci Eng, A 2006;435–436: 540–6. https://doi.org/10.1016/j.msea.2006.07.039.

[50] Yeratapally SR, Lang C, Glaessgen EH. A computational study to investigate the effect of defect geometries on the fatigue crack driving forces in powder-bed AM materials. In: AIAA Scitech 2020 Forum. Reston, Virginia: American Institute of Aeronautics and Astronautics; 2020. https://doi.org/10.2514/6.2020-1386.

[51] Sadeghirad A, Momeni K, Ji Y, Ren X, Chen L-Q, Lua J. Multiscale crystal-plasticity phase field and extended finite element methods for fatigue crack initiation and propagation modeling. Int J Fract 2019;216:41–57. https://doi.org/10.1007/s10704-018-00339-5.

[52] Prithivirajan V, Ravi P, Naragani D, Sangid MD. Direct comparison of microstructure-sensitive fatigue crack initiation via crystal plasticity simulations and in situ high-energy X-ray experiments. Mater Des 2021;197:109216. https://doi.org/10.1016/j.matdes.2020.109216.

[53] Eisenlohr P, Diehl M, Lebensohn RA, Roters F. A spectral method solution to crystal elasto-viscoplasticity at finite strains. Int J Plast 2013;46:37–53. https://doi.org/10.1016/j.ijplas.2012.09.012.

[54] Bandyopadhyay R, Prithivirajan V, Peralta AD, Sangid MD. Microstructure-sensitive critical plastic strain energy criterion for fatigue life prediction across various loading regimes. Proc R Soc A 2020;476(2236):20190766.

[55] Anahid M, Samal MK, Ghosh S. Dwell fatigue crack nucleation model based on crystal plasticity finite element simulations of polycrystalline titanium alloys. J Mech Phys Solids 2011;59:2157–76. https://doi.org/10.1016/j.jmps.2011.05.003.

[56] Yaghoobi M, Stopka KS, Lakshmanan A, Sundararaghavan V, Allison JE, McDowell DL. PRISMS-Fatigue computational framework for fatigue analysis in polycrystalline metals and alloys. npj Comput Mater 2021;7:38. https://doi.org/10.1038/s41524-021-00506-8.

[57] McDowell DL, Dunne FPE. Microstructure-sensitive computational modeling of fatigue crack formation. Int J Fatigue 2010;32:1521–42. https://doi.org/10.1016/j.ijfatigue.2010.01.003.

[58] Castelluccio GM, Musinski WD, McDowell DL. Recent developments in assessing microstructure-sensitive early stage fatigue of polycrystals. Curr Opin Solid State Mater Sci 2014;18:180–7. https://doi.org/10.1016/j.cossms.2014.03.001.

[59] Hochhalter J, Bomarito G, Yeratapally S, Leser P, Ruggles T, Warner J, et al. Non-deterministic Calibration of Crystal Plasticity Model Parameters. In: Ghosh S, Woodward C, Przybyla C, editors. Integrated Computational Materials Engineering (ICME). Cham, Switzerland: Springer; 2020. p. 165–98.

[60] Pierson KD, Hochhalter JD, Spear AD. Data-Driven Correlation Analysis Between Observed 3D Fatigue-Crack Path and Computed Fields from High-Fidelity, Crystal-Plasticity, Finite-Element Simulations. JOM 2018;70:1159–67. https://doi.org/10.1007/s11837-018-2884-2.

[61] Sangid MD. The physics of fatigue crack initiation. Int J Fatigue 2013;57:58–72. https://doi.org/10.1016/j.ijfatigue.2012.10.009.

[62] McGinty RD, McDowell DL. Multiscale Polycrystal Plasticity. J Eng Mater Technol 1999;121:203. https://doi.org/10.1115/1.2812367.

[63] Xue Y, Burton CL, Horstemeyer MF, McDowell DL, Berry JT. Multistage Fatigue Modeling of Cast A356–T6 and A380-F Aliminum Alloys. Metall Mater Trans B 2007;38:601–6.

[64] Castelluccio GM, McDowell DL. A mesoscale approach for growth of 3D microstructurally small fatigue cracks in polycrystals. Int J Damage Mech 2014;23: 791–818. https://doi.org/10.1177/1056789513513916.

[65] Roters F, Diehl M, Shanthraj P, Eisenlohr P, Reuber C, Wong SL, et al. DAMASK – The Düsseldorf Advanced Material Simulation Kit for modeling multi-physics crystal plasticity, thermal, and damage phenomena from the single crystal up to the component scale. Comput Mater Sci 2019;158:420–78. https://doi.org/10.1016/j.commatsci.2018.04.030.

[66] Hennessey C, Castelluccio GM, McDowell DL. Sensitivity of polycrystal plasticity to slip system kinematic hardening laws for Al 7075–T6. Mater Sci Eng, A 2017;687: 241–8. https://doi.org/10.1016/j.msea.2017.01.070.

[67] Dodaran MSMS, Guo S, Khonsari MMMM, Shamsaei N, Shao S. A theoretical calculation of stacking fault energy of Ni alloys: The effects of temperature and composition. Comput Mater Sci 2021;191:110326. https://doi.org/10.1016/j.commatsci.2021.110326.

[68] Dodaran M, Ettefagh AH, Guo SM, Khonsari MM, Meng WJ, Shamsaei N, et al. Effect of alloying elements on the γ` antiphase boundary energy in Ni-base superalloys. Intermetallics (Barking) 2020;117:106670.

[69] Saether E, Yamakov V, Phillips DR, Glaessgen EH. An Overview of the State of the Art in Atomistic and Multiscale Simulation of Fracture. VA: Hampton; 2009.

[70] Martin N, Ochoa N, Saï K, Hervé-Luanco E, Cailletaud G. A multiscale model for the elastoviscoplastic behavior of Directionally Solidified alloys: Application to FE structural computations. Int J Solids Struct 2014;51:1175–87. https://doi.org/10.1016/j.ijsolstr.2013.12.013.

[71] Cruzado A, LLorca J, Segurado J. Modeling cyclic deformation of inconel 718 superalloy by means of crystal plasticity and computational homogenization. Int J Solids Struct 2017;122-123:148–61.

[72] Zhang B, Dodaran MS, Shao S, Choi J, Park S, Meng WJ. Understanding of plasticity size-effect governed mechanical response and incomplete die filling in a microscale double-punch molding configuration. Int J Mech Sci 2020;172:105406.

[73] Zhang B, Dodaran M, Ahmed S, Shao S, Meng WJ, Juul KJ, et al. Grain-size affected mechanical response and deformation behavior in microscale reverse extrusion. Materialia (Oxf) 2019;6:100272. https://doi.org/10.1016/j.mtla.2019.100272.

[74] Zhang X, Mu Y, Dodaran M, Shao S, Moldovan D, Meng WJ. Mechanical failure of CrN/Cu/CrN interfacial regions under tensile loading. Acta Mater 2018;160:1–13. https://doi.org/10.1016/j.actamat.2018.08.046.

[75] Liu X, Zhao C, Zhou X, Shen Z, Liu W. Microstructure of selective laser melted AlSi10Mg alloy. Mater Des 2019;168:107677. https://doi.org/10.1016/j.matdes.2019.107677.

[76] Wang G, Ouyang H, Fan C, Guo Q, Li Z, Yan W, et al. The origin of high-density dislocations in additively manufactured metals. Mater Res Lett 2020;8:283–90. https://doi.org/10.1080/21663831.2020.1751739.

[77] Pegues JW, Roach MD, Shamsaei N. Additive manufacturing of fatigue resistant austenitic stainless steels by understanding process-structure–property relationships. Mater Res Lett 2020;8:8–15. https://doi.org/10.1080/21663831.2019.1678202.

[78] Maiti T, Eisenlohr P. Fourier-based spectral method solution to finite strain crystal plasticity with free surfaces. Scr Mater 2018;145:37–40. https://doi.org/10.1016/j.scriptamat.2017.09.047.

[79] Castelluccio GM, McDowell DL. Mesoscale modeling of microstructurally small fatigue cracks in metallic polycrystals. Mater Sci Eng, A 2014;598:34–55. https://doi.org/10.1016/j.msea.2014.01.015.

[80] ASTM E606/E606M . Standard Test Method for Strain-Controlled Fatigue Testing . ASTM International ; 2004 . https://doi.org/10.1520/E0606-04E01.

[81] Lee S, Shao S, Wells DN, Zetek M, Kepka M, Shamsaei N. Fatigue behavior and modeling of additively manufactured IN718: The effect of surface treatments and surface measurement techniques. J Mater Processing Technol 2021:117475. https://doi.org/10.1016/j.jmatprotec.2021.117475.

[82] ASTM F3055-14a . Standard Specification for Additive Manufacturing Nickel Alloy (UNS N07718) with Powder Bed Fusion . ASTM International; 2014 . https://doi.org/10.1520/F3055-14A.

[83] NASA, MSFC-SPEC-3717 - Specification for Control and Qualification of Laser Powder Bed Fusion Metallurgical Processes, (2017) 58. https://doi.org/MSFC-SPEC-3717.

[84] ASTM E3−11 . Standard Guide for Preparation of Metallographic Specimens Standard Guide for Preparation of Metallographic Specimens 1 . ASTM International; 2012 . https://doi.org/10.1520/E0003-11R17.1.

[85] Cheng AS, Laird C. Mechanisms of fatigue hardening in copper single crystals: The effects of strain amplitude and orientation. Mater Sci Eng 1981;51:111–21. https://doi.org/10.1016/0025-5416(81)90112-9.

[86] Tabata T, Fujita H, Hiraoka M-A, Onishi K. Dislocation behaviour and the formation of persistent slip bands in fatigued copper single crystals observed by high-voltage electron microscopy. Philos Mag A: Phys Condensed Matter, Struct Defects Mech Properties 1983;47(6):841–57.

[87] Polák J. Production, annihilation and migration of point defects in cyclic straining. Materialia (Oxf) 2020;14:100938.

[88] Mughrabi H, Wang R, Differt K, Essmann U. In: Fatigue Mechanisms: Advances in Quantitative Measurement of Physical Damage. 100 Barr Harbor Drive, PO Box C700, West Conshohocken, PA 19428-2959: ASTM International; 1983. 5–5-41.

[89] Mazánová V, Heczko M, Polák J. On the mechanism of fatigue crack initiation in high-angle grain boundaries. Int J Fatigue 2022;158:106721. https://doi.org/10.1016/j.ijfatigue.2022.106721.

[90] ASTM E2627 . Standard Practice for Determining Average Grain Size Using Electron Backscatter Diffraction (EBSD) in Fully Recrystallized Polycrystalline Materials . ASTM International; 2019 . https://doi.org/10.1520/E2627.